molecules

MDPI

Article

Integrating Explicit and Implicit Fullerene Models into UNRES Force Field for Protein Interaction Studies

Natalia H. Rogoża [1], Magdalena A. Krupa [1], Pawel Krupa [2,*] and Adam K. Sieradzan [1]

[1] Faculty of Chemistry, University of Gdańsk, Fahrenheit Union of Universities in Gdańsk, Bażyńskiego 8, 80-309 Gdańsk, Poland; n.rogoza.927@studms.ug.edu.pl (N.H.R.); krupa.magdalena@outlook.com (M.A.K.); adam.sieradzan@ug.edu.pl (A.K.S.)

[2] Institute of Physics, Polish Academy of Sciences, Al. Lotnikow 32/46, 02-668 Warsaw, Poland

* Correspondence: pkrupa@ifpan.edu.pl; Tel.: +48-22-116-3224

Abstract: Fullerenes, particularly C_{60}, exhibit unique properties that make them promising candidates for various applications, including drug delivery and nanomedicine. However, their interactions with biomolecules, especially proteins, remain not fully understood. This study implements both explicit and implicit C_{60} models into the UNRES coarse-grained force field, enabling the investigation of fullerene–protein interactions without the need for restraints to stabilize protein structures. The UNRES force field offers computational efficiency, allowing for longer timescale simulations while maintaining accuracy. Five model proteins were studied: FK506 binding protein, HIV-1 protease, intestinal fatty acid binding protein, PCB-binding protein, and hen egg-white lysozyme. Molecular dynamics simulations were performed with and without C_{60} to assess protein stability and investigate the impact of fullerene interactions. Analysis of contact probabilities reveals distinct interaction patterns for each protein. FK506 binding protein (1FKF) shows specific binding sites, while intestinal fatty acid binding protein (1ICN) and uteroglobin (1UTR) exhibit more generalized interactions. The explicit C_{60} model shows good agreement with all-atom simulations in predicting protein flexibility, the position of C_{60} in the binding pocket, and the estimation of effective binding energies. The integration of explicit and implicit C_{60} models into the UNRES force field, coupled with recent advances in coarse-grained modeling and multiscale approaches, provides a powerful framework for investigating protein–nanoparticle interactions at biologically relevant scales without the need to use restraints stabilizing the protein, thus allowing for large conformational changes to occur. These computational tools, in synergy with experimental techniques, can aid in understanding the mechanisms and consequences of nanoparticle–biomolecule interactions, guiding the design of nanomaterials for biomedical applications.

Keywords: molecular dynamics; coarse-graining; force fields; proteins; fullerenes; nanoparticles; nanotoxicity

Citation: Rogoża, N.R.; Krupa, M.A.; Krupa, P.; Sieradzan, A.K. Integrating Explicit and Implicit Fullerene Models into UNRES Force Field for ProteinInteraction Studies. *Molecules* **2024**, *29*, 1919. https://doi.org/10.3390/molecules29091919

Academic Editor: Teobald Kupka

Received: 26 March 2024
Revised: 16 April 2024
Accepted: 19 April 2024
Published: 23 April 2024

1. Introduction

Nanotechnology, an interdisciplinary field combining chemistry, physics, medicine, and engineering, has led to the design and implementation of various nanoparticles in recent decades [1]. Carbon-based nanoparticles, including fullerenes and carbon nanotubes, were among the first discovered and have been widely studied for their unique properties [2,3].

Among carbon nanoparticles, fullerenes are known for their spherical shape, consisting of carbon atoms connected by single and double bonds forming pentagons and hexagons [4]. The most common type is C_{60}, also known as buckminsterfullerene, built from 60 sp^2-hybridized carbon atoms [5]. It has 12 pentagonal and 20 hexagonal sides composing a structure reminiscent of a football [6] with the average diameter of about 0.71 nm [7], calculated using carbon centers of mass. C_{60} naturally occurs in low concentrations [8,9], and can be produced by human activities [10]; however, most C_{60} used today is synthetically produced, with rapidly increasing amounts [11].

C_{60} exhibits unique chemical properties. C_{60} exhibits low water solubility, which can be improved by attaching functional groups [12]. Fullerenes have high electron affinity, allowing efficient electron transport for applications like solar cells [13] and chemical sensors [14,15]. C_{60} derivatives are also used in cosmetics for antioxidative abilities [16] and they are investigated as potential drug delivery systems due to their cage-like structure [17,18].

The increasing environmental presence of C_{60} raises concerns about potential nanotoxicity from skin contact, inhalation, or ingestion [16,19,20]. While the exact fate in the human body is not fully understood [21], research indicates cellular uptake via passive diffusion and endocytosis [22]. As fullerenes enter cells, interactions with proteins should be studied.

1.1. Fullerene-Protein Interactions

Interactions of C_{60} and fullerene derivatives (FDs) with certain proteins have been experimentally proven. C_{60} fits well in the HIV-1 protease active site, potentially blocking this key enzyme [23], while monoclonal anti-C_{60} antibodies, including anti-Buckminsterfullerene Fab fragment, were isolated and the Fab fragment with specificity for C_{60} exhibited a competitive inhibition mechanism [24]. Fullerenol, a soluble hydroxylated FD, inhibits various enzymes and proteins [25–28]. Water-miscible fullerene carboxylic acid also inhibits cysteine and serine proteases [29,30]. Inhibitory effects by FDs have been observed also for several other proteins [31–35]. Docking studies have revealed new potential protein targets for C_{60} binding. Reverse docking identified FKBP and uteroglobin as top candidates [36], while another study found an FD bound to intestinal fatty acid binding protein (IFABP) [37]. Binding to these proteins may alter their activities and biological processes. In vitro experiments confirm potential harmful effects of C_{60} aggregates and fullerenols on tissues, though differences exist between in vitro toxicity and in vivo effects [38,39]. A recent in vivo mouse study found lung tissue changes, increased reactive oxygen species, and decreased ATP production after C_{60} exposure [40].

1.2. Theoretical Methods of Studying Nanoparticles

Both experimental and theoretical approaches are used to study nanoparticle properties, each providing valuable observations [41,42]. Experiments allow us to obtain general insight into nanoparticle properties, including nanotoxicity, mentioned above, as well as size, shape, composition, and stability [43]. Theoretical methods, on the other hand, might help us explain underlying mechanisms governing the nanoparticle's behavior at the molecular and quantum level within a comparatively shorter timescale. For example, in one study, a density functional theory (DFT) method, allowing the exploration of the electronic structure of molecules, was used to precisely determine the exact mode of attaching an analyzed ligand to a gold nanoparticle surface, which was not possible to characterize with experimental methods alone [44]. Another useful theoretical tool in studying nanoparticles is molecular docking, allowing the identification of nanoparticle binding sites on proteins [36]. The molecular dynamics (MD) approach is also used to study potential interactions of nanoparticles with other molecular structures. It depicts the dynamic behavior of a system over time and can be used to examine potential interactions of nanoparticles with biomolecules, for example, cell membranes [45] and proteins [46]. Furthermore, the implementation of coarse-grained models of biomolecules and nanoparticles, such as those used in the MARTINI force field [47–50], offers a significant advantage in computational efficiency, enabling longer simulations compared to the atomistic approach. However useful, it should be noted that the MARTINI 2 and 3 coarse-grained force fields cannot be effectively used to study large conformational changes of proteins [51,52], as a reference initial atomistic structure is used for generation of backbone and some side-chain parameters [53], and tertiary structure is kept mostly by the elastic network to maintain the structure [54]. This limitation can be somehow alleviated by using the Go-MARTINI variant instead of the elastic network [55].

Therefore, the main goal of this work was to implement explicit and implicit fullerene models into the UNRES force field to enable performing fullerene–protein studies with the ability to study both small and large conformational changes without the necessity to use restraints stabilizing protein structure. On the other hand, using molecular dynamics with a coarse-grained UNRES force field solves the problem of expensive all-atom calculations and allows for 3–4 orders of magnitude longer timescale simulations, while maintaining adequate accuracy.

2. Methods

2.1. UNRES Model

The UNited RESidue (UNRES) is a highly reduced protein model developed for studies of peptides and proteins. It offers a significant computational advantage, providing a four-order-of-magnitude speed-up compared to traditional all-atom simulations. In the UNRES model [56,57], a polypeptide chain is represented by a sequence of alpha-carbon (C^α) atoms connected by virtual bonds with united peptide groups (p) placed halfway between consecutive C^α atoms, and united side chains (SCs) attached to the C^α atoms. United peptide groups and united side chains serve as the primary interaction sites, while the C^α atoms are solely responsible for defining the geometry of the polypeptide chain backbone: it is specified by the C^α–C^α–C^α virtual bond angles θ and C^α–C^α–C^α–C^α virtual bond dihedral angles γ. Additionally, α and β are angles defining side-chain center local geometry (Figure 1). The UNRES force field uses a physics-based approach for simulations of protein structure and dynamics. The effective energy function arises from the potential of mean force (PMF) of the system where all degrees of freedom not belonging to the coarse-grained representation have been integrated out. It should be noted that solvent is present in an implicit form and is implemented in the effective energy function. The PMF is then approximated by the generalized Kubo cluster-cumulant series limited to the most important factors. This allows for analytical derivation of the expression for effective energy terms. The effective energy function in the UNRES force field is expressed as follows:

$$\begin{aligned} U &= w_{SC}\sum_{i<j} U_{SC_iSC_j} + w_{SCp}\sum_{i\neq j} U_{SC_ip_j} + w_{pp}^{VDW}\sum_{i<j-1} U_{p_ip_j}^{VDW} + w_{pp}^{el} f_2(T)\sum_{i<j-1} U_{p_ip_j}^{el} \\ &+ w_{tor} f_2(T)\sum_i U_{tor}(\gamma_i,\theta_i,\theta_{i+1}) + w_b\sum_i U_b(\theta_i) + w_{rot}\sum_i U_{rot}\left(\theta_i,\alpha_{SC_i},\beta_{SC_i}\right) \\ &+ w_{bond}\sum_i U_{bond}(d_i) + w_{ssbond}\sum_{n_{ss}} U_{ssbond}(d_{ss}) + w_{corr}^{(3)} f_3(T) U_{corr}^{(3)} + w_{turn}^{(3)} f_3(T) U_{turn}^{(3)} \end{aligned} \quad (1)$$

where the Us are the energy terms. The function is composed of both long-range and local terms with the addition of multibody components. The long-range components are $U_{SC_iSC_j}$ (denoting solvent-mediated side-chain–side-chain interaction energies), $U_{SC_ip_j}$ (corresponding to the excluded-volume potential of side-chain–peptide group interactions), and $U_{p_ip_j}$ (being peptide group potential split into the Lennard–Jones interaction energy between peptide group centers—$U_{p_ip_j}^{VDW}$, and the mean electrostatic energy between peptide groups terms—$U_{p_ip_j}^{el}$). Local components of the polypeptide chain include U_{tor}, U_b, U_{rot}, U_{bond}, and correspond to the backbone torsional terms, virtual bond angle terms, side-chain rotamer terms, and virtual bond deformation terms, respectively. U_{ssbond} denotes the terms corresponding to disulfide bonds potential [58]. $U_{corr}^{(3)}$ and $U_{turn}^{(3)}$ are multibody terms accounting for the coupling of the backbone–local and backbone–electrostatic interactions [59]. Energy terms in the expression are multiplied by appropriate weights (w_x), which have been re-optimized using maximum likelihood approach [60]. The values associated with factors of order greater than one are scaled by the corresponding temperature coefficients [61], which are defined by $f_n(T)$, where $T_o = 300$ K. Temperature coefficients are expressed by the following:

$$f_n(T) = \frac{\ln[\exp(1) + \exp(-1)]}{\ln\left\{\exp\left[(T/T_o)^{n-1}\right] + \exp\left[-(T/T_o)^{n-1}\right]\right\}} \quad (2)$$

UNRES is suitable for the prediction of protein structures and has performed well in biannual CASP experiments [62–65]. The model was successfully applied in protein folding research [66], free-energy landscapes studies [67], oligomerization of intrinsically disordered proteins [68], and long-time scale simulations of big systems, for example, virus-like particles [69]. An extension to analyze the binding of proteins to carbon nanotubes using an implicit representation of the nanoparticle has also been developed [70] and used to study their impact on model proteins.

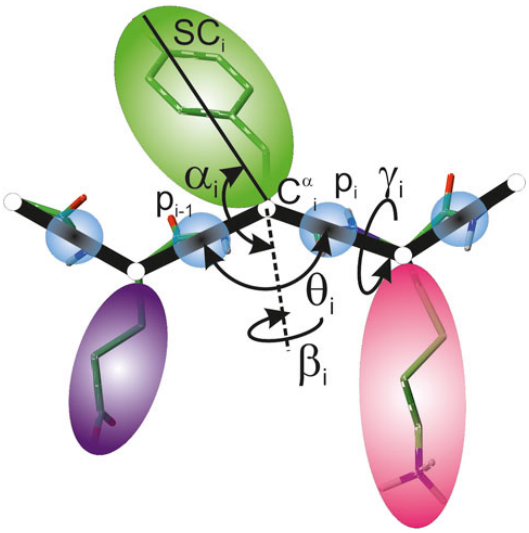

Figure 1. A scheme of polypeptide chain representation in the UNRES model [71]. United peptide groups (p) (blue spheres) and united side chains (SC) (spheroids of different colors) attached to C^α atoms are the interaction sites. Geometry of the backbone is defined by C^α–C^α–C^α virtual bond angles θ and C^α–C^α–C^α–C^α virtual bond dihedral angles γ. SC_i center local geometry is defined by the angle between bisection of θ_i and the C^α_i–SC_i vector (α_i angle), and the angle of rotation of the C^α_i–SC_i vector from C^α_{i-1}–C^α_i–C^α_{i+1} plane (β_i angle).

2.2. C_{60} Model in UNRES Force Field

In this work, we introduced two types of nanospheres to model C_{60} fullerene: implicit and explicit. It should be noted that the implicit model cannot freely move during simulations; however, other molecules, e.g., peptides and proteins, can move around it, while the explicit model allows for full mobility.

2.2.1. Explicit Model

In the explicit model of the C_{60}, the fullerene nanoparticle is approximated by 20 alanine side chains (Figure 2B). The alanine side chain was chosen as it is the smallest amino acid that has a side chain with hydrophobic character, similar to C_{60}. The number of centers (20) was the maximum number of interaction centers that could be used to approximate C_{60} that remained stable (24 and a larger number of centers were tested, leading to instability of the nanoparticle due to steric clashes). The initial positions of 20 centers are in the form of a regular dodecahedron. It should be noted that no peptide group is present between alanines; however, Cα atoms are present, and face inward toward the nanoparticle and serve as anchors of restraints imposed. Between any two Cα atoms in the fullerene, harmonic restraints were imposed, with the force constant value 10 kcal mol^{-1}Å^{-2} to maintain a sphere-like shape. As the Cα-SC are connected via U_{bond}, this allows small distortions of the nanoparticle. As each of the 20 centers is treated separately, there are no U_{tor} or U_{ang} energy terms describing nanoparticle behavior. It should be noted that there

is no explicit water–nanoparticle interaction; however, those interactions are implicitly incorporated in the alanine side-chain potentials of mean force. The explicit model of the implemented C_{60} fullerene is based on alanine side chains and interacts with the protein through the Gay–Berne potential (anisotropic modification of the Lennard–Jones potential) (Equation (3)):

$$E_{Gay-Berne} = 4\epsilon[(\frac{\sigma_0}{r-\sigma+\sigma_0})^{12} - (\frac{\sigma_0}{r-\sigma+\sigma_0})^{6}] \quad (3)$$

where r is the distance between the centers of the side chains, σ is the distance corresponding to the zero value of $E_{Gay-Berne}$ for an arbitrary orientation of the particles (σ_0 is the distance corresponding to the zero value of $E_{Gay--Berne}$ for a side-to-side orientation), and ϵ (depending on the relative orientation of the particles) is the van der Waals well depth. For a detailed description, see ref. [72]. The parameters for Equation (3) are shown in Supplementary Table S1.

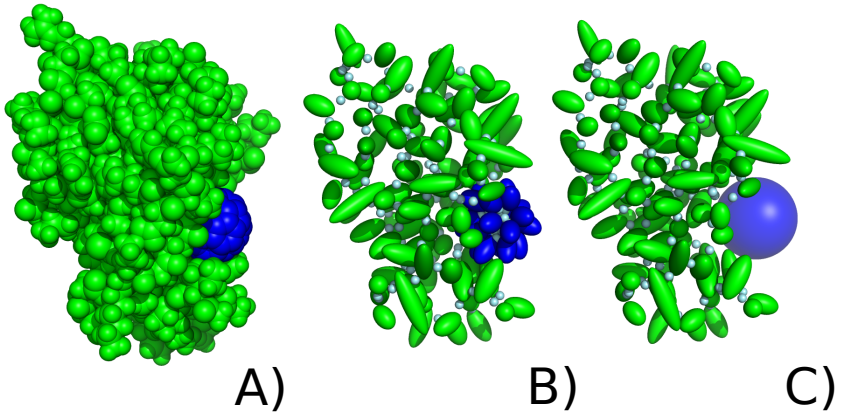

Figure 2. FK506 binding protein (green) with C_{60} fullerene (blue) in (**A**) all-atom representation, (**B**) UNRES coarse-grained protein representation with explicit coarse-grained fullerene representation, (**C**) UNRES coarse-grained protein representation with implicit coarse-grained fullerene.

2.2.2. Implicit Model of Nanoparticle Representation

In the implicit form, the nanoparticle is approximated as a sphere that occupies a given space of a periodic box (Figure 2C). It should be noted that the nanoparticle is immobile and always occupies the same user-defined part of the box; however, other molecules can move around it. The size and shape of the nanosphere are also predetermined and do not change during the course of a simulation; however, it is reasonable in the case of a rigid C_{60}. The implicit model of nanosphere allows only to simulate one nanoparticle at a time; however, this representation allows for extremely fast computation. As in case of the explicit nanoparticle, there is no explicit water–nanoparticle interaction; however, those interactions are implicitly incorporated in the protein–nanoparticle potentials of mean force (in σ and ϵ parameters).

The protein-nanoparticle interactions are described by the Kihara potential [73]:

$$U_{\text{prot-nano}} = 4\epsilon\left[\left(\frac{\sigma}{r-R_0}\right)^{12} - \left(\frac{\sigma}{r-R_0}\right)^{6}\right] \quad (4)$$

where ϵ is the interaction potential well depth, σ is the distance where the interaction potential obtains value 0, r is the distance between the protein center of interaction (p_i or SC_i) and the center of the nanosphere, and R_0 is the size of the nanoparticle. In this particular article, the parameters (ϵ and σ) for interaction with the protein were taken from the phenylalanine side-chain model to approximate the fullerene (Supplementary Table S1); however, the application of this nanoparticle model can be extended to various nanoparticles by adjusting the size and the ϵ and σ. The modeled C_{60} had R_0 set to 3.5 Å.

2.3. Protein Selection

To study interactions of proteins with fullerenes, five model systems for which there are suggestions that they can interact with C_{60} fullerene or its derivatives were selected: FK506 binding protein (PDB ID: 1FKF), HIV-1 protease (PDB ID: 1HOS), intestinal fatty acid binding protein (PDB ID: 1ICN), PCB-binding protein (PDB ID: 1UTR), and hen egg-white lysozyme (PDB ID: 1DPX) [36,37,74]. The last was studied in two alternative versions to examine the impact of disulfide residues on the system stability and behavior: with all disulfide bonds present, marked as $1DPX_{SS}$, and without disulfide bonds, marked as $1DPX_{no\ SS}$. It should be noted that dynamic disulfide bond treatment was used, which allows disulfide bonds to break and form during simulations and it is one of the unique features, which can be combined with newly-implemented C_{60} fullerene models [75]. As a reference, a set of UNRES simulations for each of the abovementioned proteins was run without the C_{60} present. These proteins were selected as the previous studies indicated that they can interact with C_{60} fullerene or its derivatives and have relatively small size, which allowed for the comparison with all-atom results, various fold-types and secondary structure contents (1FKF, 1HOS, and 1ICN are mostly formed by β-strands, while 1UTR and 1DPX are mostly helical) and various biological roles played in the organisms. Together, the selected protein set should allow for simple, yet comprehensive, tests of the implemented C_{60} fullerene models.

2.4. MD Simulation Details

2.4.1. Coarse-Grained UNRES Simulations

Three different approaches of molecular dynamics (MD) simulations were used in the UNRES force field for each of the selected proteins:

1. Without fullerene nanoparticle (to assess protein stability);
2. With implicit model of fullerene nanoparticle;
3. With explicit model of fullerene nanoparticle.

The starting protein structures were the same as in all-atom Amber simulations after energy minimization. While not strictly required, it was applied for further comparative purposes of coarse-grained and all-atom approaches. Energy minimization of these starting structures in UNRES was carried out with the SUMSL algorithm [76]. All the simulations were conducted with the Berendsen thermostat at 260 K, as the temperature in UNRES is not yet fully optimized and 260 K is recommended [77]. The number of steps in each simulation was set to 4,000,000, which, with a time step of 4.89 fs and 1000 times speed-up of the UNRES force field, resulted in almost ∼20 µs laboratory time long simulations. A total of 20 trajectories were run for each type of approach for each protein, totaling about ∼400 µs for each system variant.

2.4.2. All-Atom Amber Simulations

For comparison, we conducted individual 1000 ns molecular dynamics (MD) simulations on selected proteins with and without a C_{60} fullerene particle using Amber22 [78] with GPU implementation. AnteChamber was employed to obtain the C_{60} molecule parameters, taking advantage of the carbon-only molecule's rigid nature, eliminating the need for sophisticated tools for charge estimation or conformational optimization. Bond and angle parameters were derived from the ff19sb [79] protein and GAFF [80] general force fields. The manual placement of C_{60} in protein binding pockets was performed using PyMol. These conformations were then surrounded by water molecules modeled using the four-point OPC water model [81]. The system was configured as a truncated octahedron periodic boundary box with a minimum water layer thickness of 15 Å. To neutralize the charge, Na^+ or Cl^- ions were added, and the system underwent parameter and topology file generation using tLeap, part of AmberTools23 [82]. Solvated proteins underwent energy minimization (10,000 steps in total, utilizing 4000 and 6000 steps with steepest descent and conjugate gradient algorithms, respectively), followed by heating and equilibration in the NPT ensemble over 1 ns with a time step of 1 fs. Subsequently, 1000 ns conventional

MD simulations with a time step of 2 fs were conducted in the NVT ensemble with GPU-compatible calculations, saving snapshots every 100 ps. Nonbonded interactions were treated with the PME method, and the cutoff value was set to 9 Å while the temperature of 300 K was maintained by the Langevin thermostat. A parallel set of simulations without the C_{60} fullerene was also performed. To investigate the impact of disulfide residues on system dynamics and stability, lysozyme was simulated in two variants: one with all disulfide bonds present and another with all disulfide bonds absent.

2.5. Analysis

2.5.1. Binding Energy Estimation

As a part of the study, binding energies between the protein and C_{60} fullerene were estimated. In the implicit model of fullerene in UNRES, the binding energy results directly from the interaction potential, while in the explicit model, the energy of the complex (E_{complex}) was obtained directly from the simulation. Meanwhile, the energies of the protein (E_{protein}) and the C_{60} nanoparticle (E_{nano}) in bulk water (implicit solvent) were calculated based on the same conformations as in the complex. The final binding energy was then calculated as

$$E_{\text{binding}} = E_{\text{complex}} - (E_{\text{protein}} + E_{\text{nano}}) \tag{5}$$

For all-atom simulations, the Molecular Mechanics with Generalized Born and Surface Area Solvation (MM-GBSA) method was used to estimate binding energies between selected proteins and C_{60} fullerene using 100 snapshots evenly distributed from the second halves of the trajectories [83]. This procedure is analogous to the one performed for the explicit C_{60} model, with a single difference: as the all-atom simulations were run in an explicit solvent model, the conversion to an implicit solvent in MM-GBSA calculations adds solvation entropy to the results, which is not present for coarse-grained UNRES simulations as UNRES employs an implicit solvent in both MD simulations and analysis. Therefore, the obtained enthalpy of binding ΔH is often called the effective binding energy. Additionally, the normal-mode analysis of harmonic frequencies method was used to predict the entropic contribution based on five snapshots per system due to the high computational cost of the method, providing Gibbs free energy:

$$\Delta G = \Delta H - T\Delta S \tag{6}$$

where ΔG is the binding free energy, ΔH is the enthalpy of binding or effective binding energy, T is temperature, and ΔS is the entropy change of the system upon complex formation.

2.5.2. All-Atom Structure Reconstruction

In order to further compare all-atom results with coarse-grained ones, the UNRES protein trajectories were first converted into all-atom representation using the PULCHRA tool [84]. Missing hydrogen atoms were added with the tLeap program. In the case of C_{60} in explicit simulations, the multi-alanine representation was replaced with an all-atom equilibrated one, based on the geometrical centers of these. For the implicit fullerene model, the all-atom C_{60} structure was inserted in the place of an approximated nanoparticle, based on the geometrical centers of the all-atom structure and the immobile nanosphere.

2.5.3. CPPTRAJ Analysis

To evaluate properties of proteins and C_{60} during simulations, an analysis with the CPPTRAJ program [85] from AmberTools23 [82] was conducted for both all-atom and reconstructed UNRES trajectories. It included calculations for root mean square deviation (RMSD) for Cα atoms, mass-weighted root mean square fluctuation (RMSF) for Cα atoms, and radius of gyration with maximum radius of gyration, both for Cα atoms. Moreover, the solvent-accessible surface area (SASA) values for all atoms were calculated for protein structures (in all simulations), as well as for protein–fullerene complexes and for single

C_{60} molecules (in simulations with C_{60}). Additionally, native contacts analysis was run. The contact cut-off distance was set to 8 Å. If a given C_{60} interaction center was within an established cut-off distance to any protein atom, it was considered to be in contact. In addition, average numbers of residues in given secondary structure were obtained.

2.5.4. Contact Probability

To analyze the stability of C_{60} binding to proteins over time, the evaluation of contact probabilities of given protein residues with explicitly defined fullerene nanoparticle during MD simulations in the UNRES force field was conducted. It was calculated from two perspectives: that of the fullerene and that of the protein, with a contact cut-off distance between residues and centers of interactions of 8 Å. Each final contact probability value was then obtained as an average from all 20 trajectories.

3. Results

3.1. Stability of a Nanoparticle in a Complex

As the selected proteins are known to interact with fullerenes and FDs, we first analyzed the stability of the C_{60} fullerene in the protein binding pockets. Figure S1 shows that high contact probabilities (close to or equal to 1) were observed for all 20 nanoparticle interaction centers in 1HOS, 1ICN, and 1UTR. Additionally, for 1FKF, an interesting contact pattern can be observed. Smaller values (0.5–1) are visible along the time axis, but at no stage is dissociation observed (at least one center from a nanoparticle has contact probability 1). This may be explained by a consistent rotation of the protein around a C_{60} molecule buried in a shallow binding pocket. Low contact probabilities are visible for the 1DPX protein ($1DPX_{no\ SS}$, $1DPX_{SS}$), where dissociation of the protein–nanoparticle complex was observed in some trajectories.

Plots of contact probabilities from the protein residues' point of view (Figure S2) reveal nonspecific binding of a nanoparticle to the 1DPX protein (Figure S2E,F). For the rest of the proteins, the interaction pattern is more specific.

For the FKBP protein (1FKF) (Figure S2A), four residues maintained constant contact with the C_{60} nanoparticle during each of the 20 MD trajectories: Tyr26, Phe46, Leu74, and Phe99. Some protein residues formed contact during the course of the simulation, which generally remained stable until the end (Val4, Val24, Met49, Pro88, Gly89, Val101). In contrast, several residues lost their initial contact with C_{60} (Phe36, Ile56, Trp59, Ile76, Tyr82, His87, Ile90). The constant contact results for Tyr26, Phe46, and Phe99 agree with experimental findings. An X-ray crystallography study of the FKBP-FK506 complex revealed a shallow binding cavity, with the side chains of Tyr26, Phe46, Phe99, Val55, and Ile56 building the sides of the hydrophobic pocket [86]. Based on these results, together with MD trajectory visualization analysis in PyMOL, C_{60} indeed remained within the binding pocket of FKBP throughout all simulations. All these observations are in agreement with the results obtained from all-atom trajectories.

The HIV-1 protease (1HOS) is a homodimeric enzyme; hence, contact probabilities for monomers A and B were plotted separately (Figure S2B). Similar interaction patterns are noticeable for both chains. For each monomer, three large protein fragments with significant contact probability values are visible. They correspond to specific parts of the protein that keep the C_{60} molecule in the enzyme's binding site. Starting from the beginning of the protein sequence, in the first group, the residues with the most probable contacts with C_{60} throughout all simulations were Asp25, Ala28, and Val32. In the second segment, residues Ile47-Gly49, Ile54, and Val56 maintained constant contact with C_{60} during the majority of simulations; however, for Ile54 and Val56, the contacts were more probable for chain B. The third section shows Leu76-Thr80 and Ile84 residues as the most probable, with Gly78-Thr80 being more probable in chain B. The experimental active site of the HIV-1 protease consists of residues Asp25-Gly27, which in this analysis corresponds to the first group. Another important part of the HIV-1 protease is the so-called flaps. They shield the enzyme's active site, built from residues Lys43 to Gln58 [87], belonging to the second group here. Moreover,

residues Val77-Val82, belonging to the third group in this analysis, were associated with conformational changes causing narrowing of the active site cavity [88]. Taking all findings into account, the C_{60} nanoparticle stayed in the HIV-1 protease's active site during course of MD simulations.

For the IFABP protein (1ICN), particular residues building an internal channel identified as the binding site in one study [89] were mostly the ones that maintained contact with the C_{60} nanoparticle in our simulations: Trp6, Val8, Tyr14, Phe17, Met18, Met21, Ile23, Leu36, Leu38, Val49, Lys50, Glu51, Ile58, Val60, Phe62, Phe68, Tyr70, Trp82, Leu89, Gly91, Phe93, Ala104, Val105, Gln106, Gln115, Thr116, Tyr117, Arg126, and Phe128 (Figure S2C).

Similarly to 1HOS, probabilities for both monomers of uteroglobin (1UTR) were plotted separately (Figure S2D). The same residues in both chains remained in constant contact with a nanoparticle: Phe5, Leu9, Leu12, Leu13, Leu40, Leu43, Val44, Leu47, Ile55, and Thr59. This agrees with experimental results, where the same residues created active sites for polychlorinated biphenyl molecule [90].

In the case of lysozyme (1DPX), the number of interactions between the protein and the explicit C_{60} fullerene model is significantly lower than for the other studied proteins. This trend agrees with the all-atom simulations, in which this protein interacts in the least strong manner. However, this observation does not agree with implicit C_{60} simulations, in which it interacted strongly in the majority of the simulations. The interactions are mainly maintained by residues 60–63 for reduced lysozyme and 60–63 along with 106–111 fragment when disulfide bonds are present.

In general, results for explicit C_{60} representation are in agreement with experimental findings on potential binding of fullerene to the studied proteins [36,37].

3.2. Strength of the Protein–Nanoparticle Interaction

Estimated binding energies (Table 1) were different for protein–C_{60} complexes in each of the approaches. Relatively lower values were observed for the implicit representation, followed by the all-atom representation, and the highest values were obtained with the explicit model. A correlation trend is visible in the data—there is a strong linear correlation between energy (R^2 = 0.97) values from all-atom and UNRES explicit C_{60} simulations (Figure 3A). Hence, all binding energies from all-atom simulations of protein binding to C_{60} are in good agreement with energies obtained from simulations with the explicit representation of the nanoparticle. It should be noted that in the case of the $1DPX_{SS}$ simulation, the average interaction energy is positive, indicating repulsion between the nanoparticle and lysozyme. This suggests that the nanoparticle is only kinetically bound to the lysozyme and cannot overcome the dissociation barrier in certain trajectories.

Table 1. Average energy of interaction between C_{60} fullerene in implicit and explicit representations in UNRES coarse-grained force field and in all-atom representation in Amber force field (ΔH stands for effective binding energy, while ΔG is Gibbs free energy).

Protein	Energy [kcal/mol]			
	UNRES		Amber	
	Implicit C_{60}	Explicit C_{60}	ΔH	ΔG
1FKF	−58.29 ± 3.67	−30.33 ± 4.82	−49.02 ± 3.95	−28.55± 5.40
1HOS	−70.58 ± 3.67	−35.28 ± 6.23	−48.66 ± 2.99	−29.40± 6.16
1ICN	−84.48 ± 3.62	−53.96 ± 4.75	−59.83 ± 2.78	−41.36 ± 3.50
1UTR	−90.48 ± 4.15	−61.81 ± 6.22	−70.87 ± 3.81	−50.18 ±.6.27
$1DPX_{no\ SS}$	−73.00 ± 10.45	−3.46 ± 5.56 *	−24.63 ± 2.15	−8.79 ± 3.67
$1DPX_{SS}$	−60.32 ± 7.85	6.24 ± 5.59 *	−23.26 ± 3.29	−9.06 ± 2.34

* The averages are calculated only for trajectories in which dissociation was not observed.

Similar observations are not applicable to the implicit approach, particularly because of the strong binding of C_{60} to the 1DPX protein (both $1DPX_{no\ SS}$ and $1DPX_{SS}$), which was not observed in the other methods. This leads to a lowering of correlation (R^2 = 0.44); if the

1DPX protein is excluded, a high correlation is observed (R^2 = 0.95). This indicates that the implicit model generally gives good binding energies but in some cases can overestimate the binding strength.

Even higher correlation is observed when the entropy contribution is included in the binding energy in the all-atom force field (Figure 3B). The correlation coefficients are R^2 = 0.98 and R^2 = 0.52 for the explicit and implicit models of the nanoparticle, respectively. This is quite understandable, as in the UNRES force field, the energy function is based on PMF, which contains an entropy contribution from averaging out the omitted degrees of freedom, also called restricted free energy. This also indicates that entropy plays an important role in nanoparticle binding.

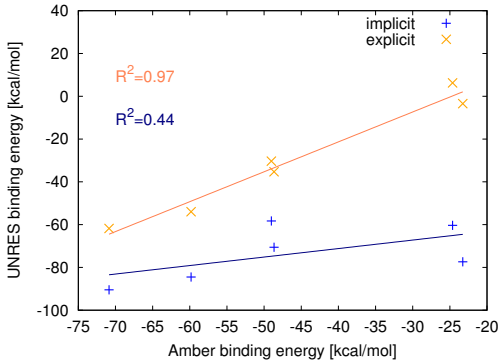

(**A**)

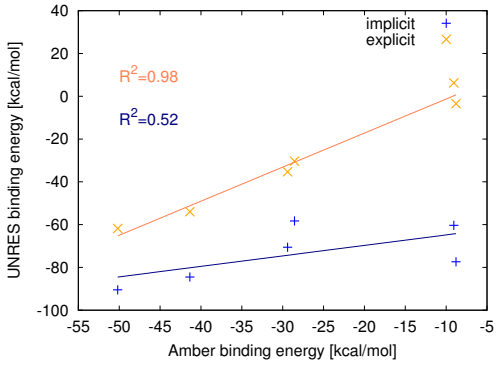

(**B**)

Figure 3. Correlation between average energy of interaction between C_{60} fullerene in implicit (blue) or explicit (orange) representations in the UNRES coarse-grained force field and ΔH (**A**) and ΔG (**B**) in the all-atom representation in the Amber force field.

The strength of binding is connected to the number of C_{60} interactions with protein residues over time for explicit simulations (Figure S1). All nanoparticle centers were in constant contact with protein residues for 1ICN and 1UTR (Figure S1C,D), which were the proteins with the strongest binding. A slightly weaker interaction was identified for the 1HOS protein, where the majority of the contact was preserved during simulations (Figure S1B). Similarly, smaller contact probability values correspond to higher energy observed for 1FKF (Figure S1A) and 1DPX (Figure S1E,F).

3.3. Nanoparticle Impact on Protein Structure

Analysis of the RMSD shows that the presence of the C_{60} fullerene does not significantly destabilize any of the analyzed proteins in any of the simulation schemes (Figure 4). Some small destabilizations upon C_{60} binding may be observed for 1KFK and 1ICN in all-atom trajectories; however, these differences are negligible and are probably attributed to normal fluctuations of the protein chain at room temperature. However, in the case of all-atom simulations of 1DPX without the disulfide bonds present, a strong opposite effect

is observed, as the presence of C_{60} fullerene stabilizes the protein structure. It should be noted, though, that this effect may simply be a result of slowing down the partial unfolding process occurring in the absence of disulfide bonds in the all-atom force field and would be observed if a sufficient timescale of simulations were reached, as most proteins are known to be semistable in the absence of some, or even all, disulfide bonds. This is further confirmed by the lack of the C_{60} effect on the stability of lysozyme in coarse-grained simulations. It should be noted that higher RMSD values are observed for the coarse-grained simulations than all-atom, which is caused by the simplified representation of proteins in the UNRES model, longer computational timescales, averaging over 20 trajectories, and inaccuracies in the reconstruction to all-atom representations. However, UNRES is known for accurately capturing protein behavior and ligand binding [91,92], despite the low resolution of the structures.

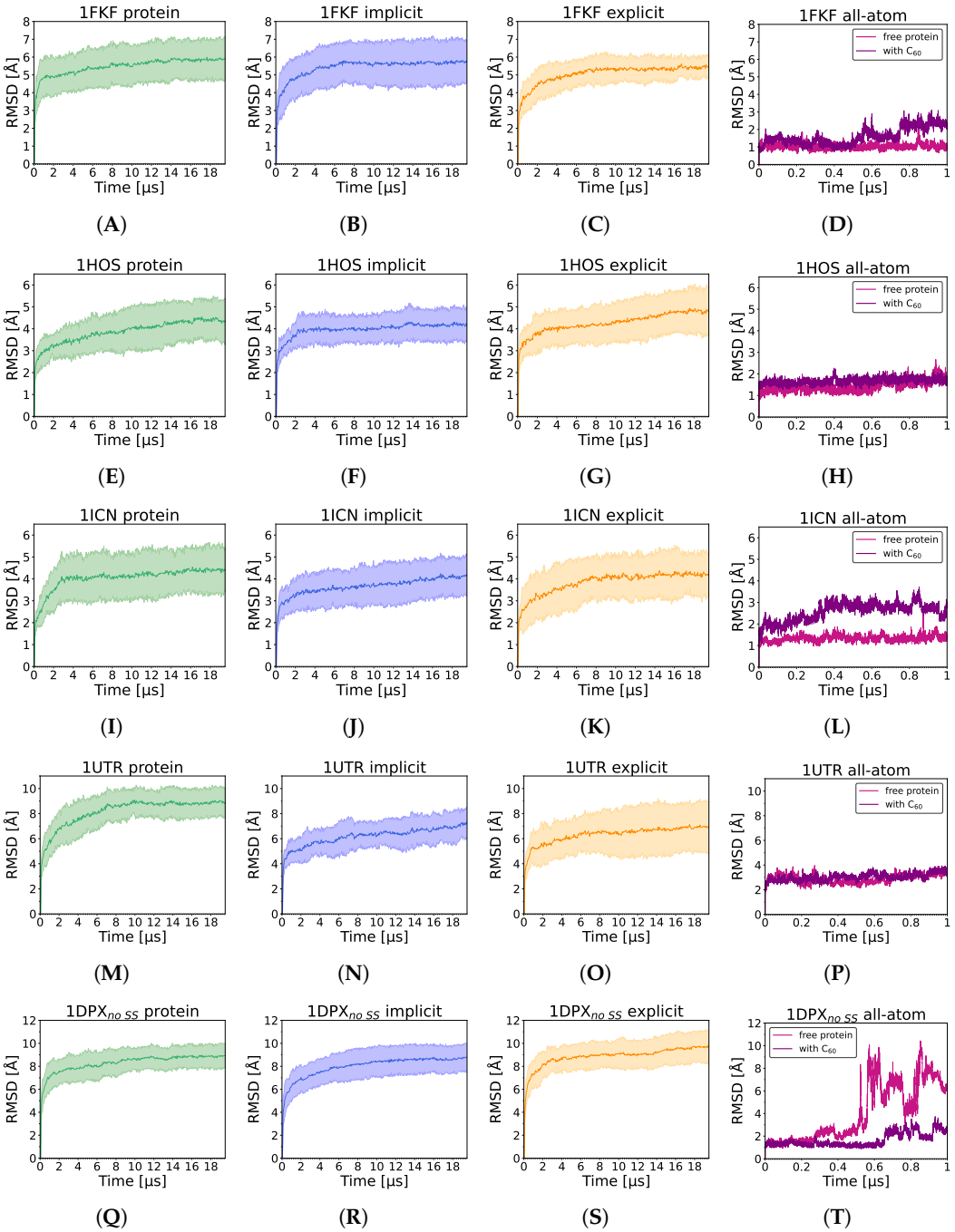

Figure 4. *Cont.*

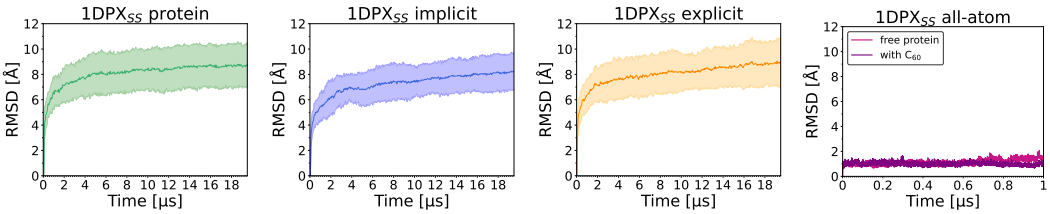

(**U**) (**V**) (**W**) (**X**)

Figure 4. RMSD values for 1FKF (**A**–**D**), 1HOS (**E**–**H**), 1ICN (**I**–**L**), 1UTR (**M**–**P**), 1DPX$_{no\ SS}$ (**Q**–**T**), and 1DPX$_{SS}$ (**U**–**X**) protein performed with UNRES force field in simulations of protein alone (green), implicit (blue), explicit (orange) simulations (averaged over 20 trajectories), and with Amber all-atom simulation of protein alone (pink) and of protein with C_{60} (purple). For simulations performed with the UNRES force field, the straight line represents the average value, while the shaded area along the line corresponds to its standard deviation.

When the influence of the nanoparticle on individual residue is analyzed (RMSF plots; Figure 5) the UNRES force field in general reveals larger fluctuations than observed in all-atom, probably as the longer simulations and, therefore, larger conformation changes could be observed. The largest differences are observed for the C-terminal fragment during all-atom 1DPX simulations without disulfide bonds; however, those changes are not confirmed by UNRES simulations. In the case of 1FKF, the largest difference is observed for region 55–65 (Figure 5A). This region is in contact with fullerene in some trajectories while losing contact in others, which might lead to conformation diversity in this region. In the 1HOS protein (Figure 5B), residues 45–55 are stabilized by fullerene, while in the UNRES force field, this region was destabilized on average by C_{60}; however, in many trajectories, stabilization could be observed as it has an extremely wide distribution in that region. For the 1ICN protein (Figure 5C) in both all-atom and UNRES simulation, region 53–58 is destabilized by the nanoparticle. In the case of the 1UTR, no significant influence of the nanoparticle on fluctuation could be observed.

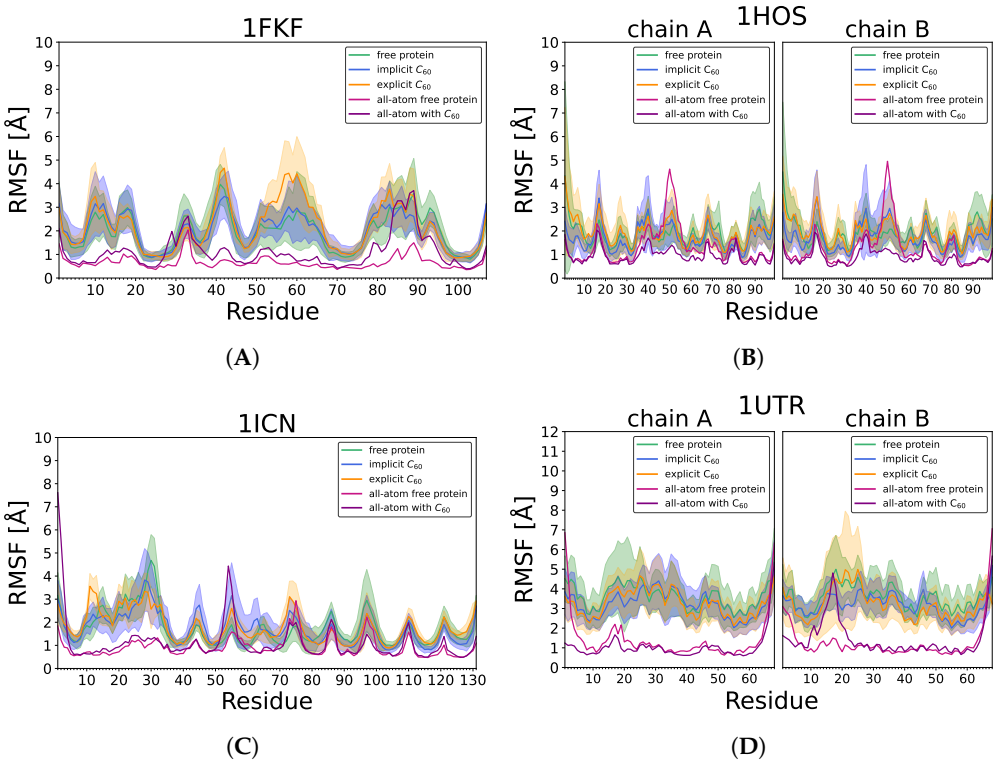

(**A**) (**B**) (**C**) (**D**)

Figure 5. *Cont.*

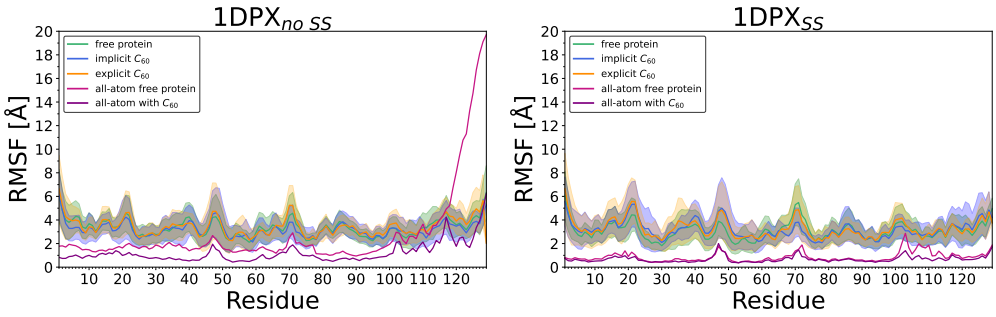

(**E**) (**F**)

Figure 5. Cα RMSF values in protein-only, implicit and explicit simulations (averaged over 20 trajectories), and during single all-atom simulations in Amber (without and with C_{60}) for (**A**) 1FKF, (**B**) 1HOS, (**C**) 1ICN, (**D**) 1UTR, (**E**) 1DPX$_{no\ SS}$, and (**F**) 1DPX$_{SS}$. For protein-only, implicit, and explicit simulations, the straight line represents the average value, while the shaded area along the line corresponds to its standard deviation.

Based on the average number of residues in a given secondary structure among all simulations with different approaches (Figure 6), we see that for all proteins, alpha and beta secondary structures remained, which, together with the lack of significant changes in observed radii of gyration (Figure 7), indicates that nanoparticle binding did not denature the protein. All-atom results for all proteins are mostly in agreement with the initial distribution of secondary structure; however, the UNRES force field tends to slightly distort secondary structure, which is visible for the 1HOS protein in Figure 6B, where the number of residues building the beta-sheet structure decreased. This effect is also attributed to the imperfection of the all-atom reconstruction and the way the DSSP algorithm predicts secondary structure elements based mostly on the hydrogen bond network, which is especially prone to inaccuracies during all-atom structure reconstruction.

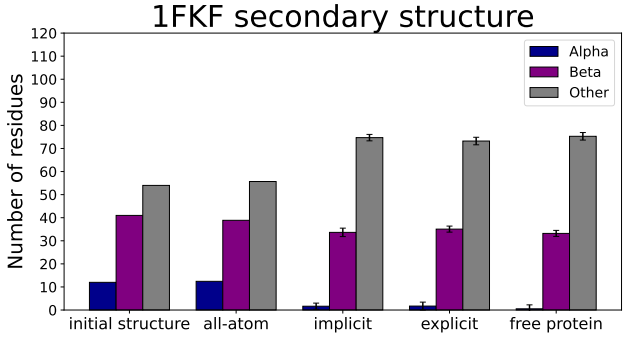

(**A**)

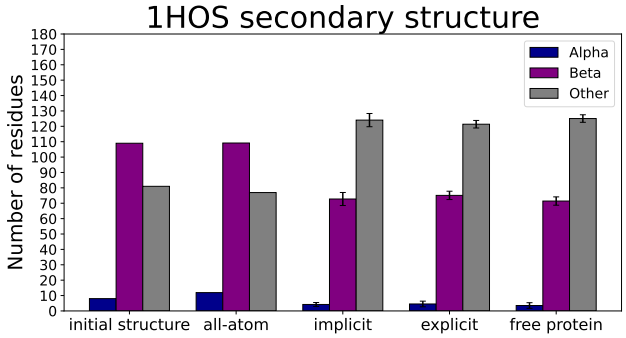

(**B**)

Figure 6. *Cont.*

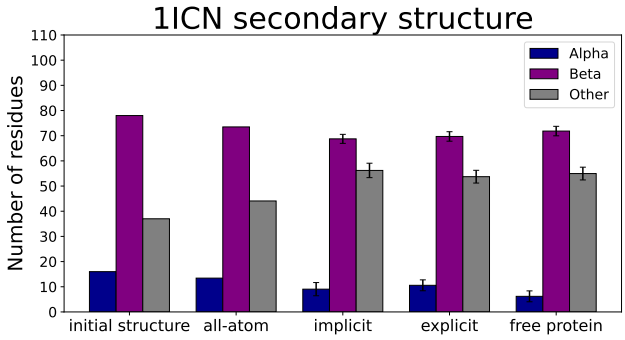

(**C**)

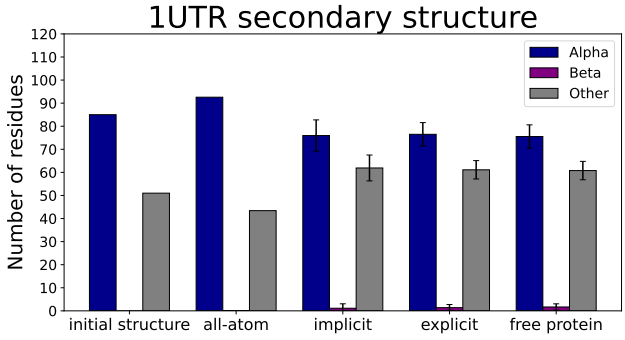

(**D**)

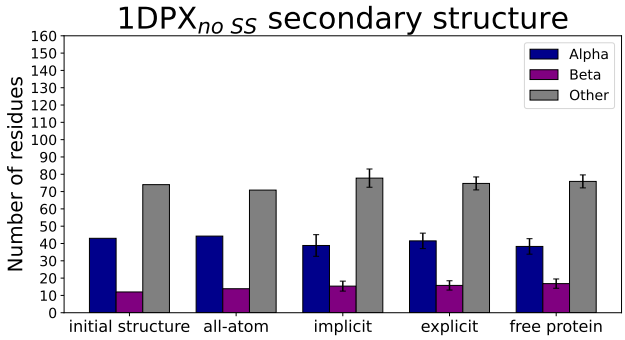

(**E**)

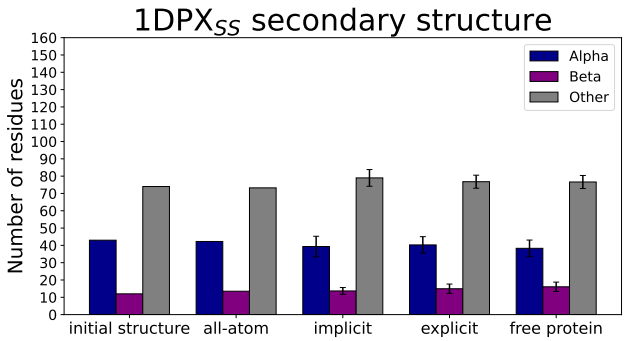

(**F**)

Figure 6. Number of residues (for initial protein structure) and average values of residues (for all-atom simulation with C_{60} in Amber force field, implicit, explicit simulations with C_{60} and protein-only simulations in UNRES coarse-grained force field) in given secondary structure for (**A**) 1FKF, (**B**) 1HOS, (**C**) 1ICN, (**D**) 1HOS, (**E**) 1DPX$_{no\ SS}$, and (**F**) 1DPX$_{SS}$. Values for UNRES simulations were averaged over 20 trajectories.

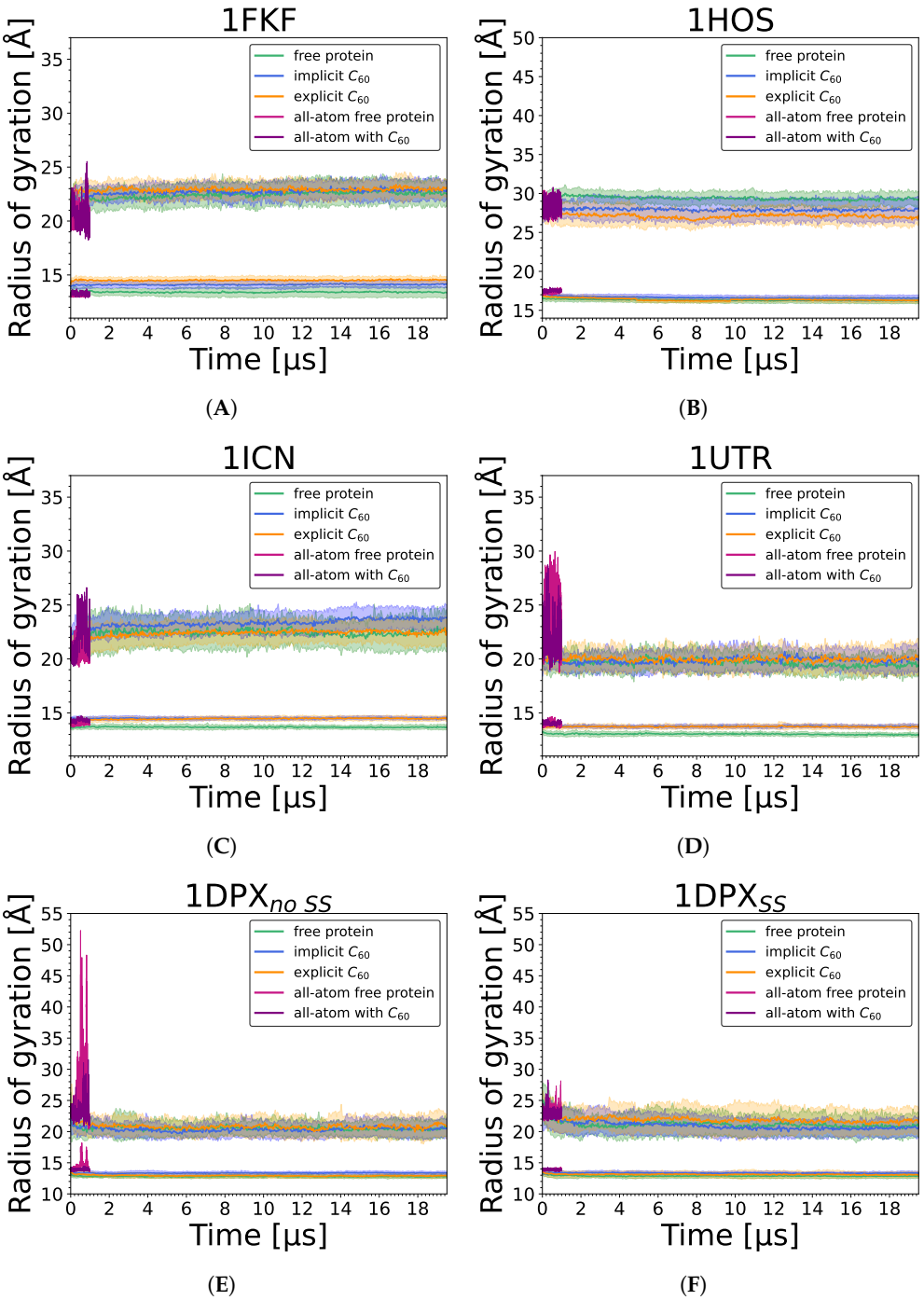

Figure 7. Changes in radius of gyration (bottom lines) and maximum radius of gyration (top lines) during protein-only, implicit and explicit simulations (averaged over 20 trajectories), and during single all-atom simulations in Amber (without and with C_{60}) for (**A**) 1FKF, (**B**) 1HOS, (**C**) 1ICN, (**D**) 1UTR, (**E**) 1DPX$_{no\ SS}$, and (**F**) 1DPX$_{SS}$. For protein-only, implicit, and explicit simulations, the straight line represents the average value, while the shaded area along the line corresponds to its standard deviation.

Analysis of SASA values shows that the UNRES reconstructed model possesses constant but 30% higher values than all-atom models (Figure 8). This effect is attributed to the imperfection of the all-atom reconstruction and the tendency of the UNRES coarse-grained force field to make proteins more soluble. Interestingly, there is about 10% higher SASA for protein when a nanoparticle is present, indicating that the nanoparticle prevents the collapse of hydrophobic residues that are in contact with that nanoparticle. Moreover, in

most cases, the addition of the nanoparticle does not increase overall SASA. Interestingly, we found no correlation between SASA increase due to the presence of the nanoparticle and the number of contacts (Figure 9). However, there is a visible relation between the number of contacts and the strength of interaction, as the weakest interaction is lysozyme (1DPX), followed by the 1FKF protein, and at the same time, 1DPX reveals the lowest number of contacts followed by 1FKF. It should be noted that the more generalized interaction site, where plenty of hydrophobic contacts can be formed, exhibits stronger binding affinity (1ICN and 1UTR) than the specific binding pocket, in which both hydrophobic and electrostatic interactions are normally formed with the ligand (1FKF and 1DPX). Therefore, it seems that the FDs would exhibit stronger binding affinity to binding pockets than C_{60}; however, they may still lack elasticity to form strong interactions within well-defined binding pockets. The largest difference in the number of contacts between all-atom and coarse-grained simulations is observed for the 1HOS protein; this difference arises from the depth of penetration of the nanoparticle. In all-atom simulations, the nanoparticle is deeply buried, while in the UNRES simulation it is surface-bound (Figure 10). The low number of contacts for 1DPX is also visible in the representative structure, where the nanoparticle is barely bound. It should be noted that in some cases (1ICN and 1UTR), the nanoparticle can penetrate deeply into the protein structure, similarily to the all-atom simulations.

The presence of the C_{60} fullerene has a very limited impact on disulfide bond stability during MD simulations (Figure 11), both in simulations with implicit and explicit C_{60} models. The only small difference can be seen in the presence of the implicit C_{60} model, which destabilizes the least stable disulfide bond, Cys64-Cys80. In general, all of the disulfide bonds are stable during simulations, keeping the respective parts of the protein close to each other. In simulations without the disulfide bonds, these parts tend to slightly rearrange, not resulting in a significant increase in the RMSD, but, nevertheless, increasing the distance between the sulfur atoms to about 10 Å for Cys30-Cys115, Cys64-Cys80, and Cys76-Cys94, and 15 Å for Cys6-Cys127. The largest distance for the latter is caused by the fact that the cysteine residues involved in this disulfide bond are placed in the most distant parts of the protein. Interestingly, a nanoparticle, when simulated in an coarse-grained explicit form, seems to have a small but noticeable stabilizing impact on the region in which Cys6 and Cys127 are present, when disulfide bonds are absent. A similar effect is observed in all-atom simulations without disulfide bonds—the presence of the C_{60} fullerene stabilizes the C-terminal part of the protein (Figure 5), which is normally rigidified by the Cys6-Cys127 disulfide bond. It should be noted that due to the imperfections of the all-atom reconstruction, even with the presence of the disulfide bond, the distance between sulfur atoms is equal to about 4 Å, instead of the typical all-atom distance of 2.05 Å.

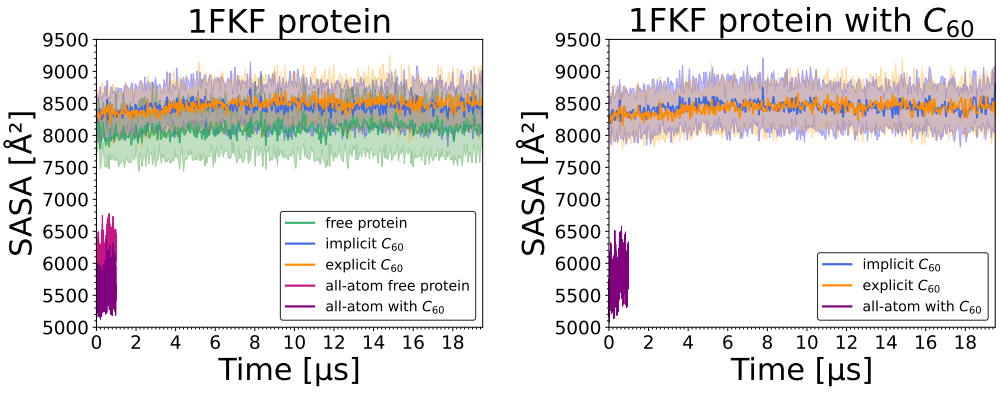

(**A**) (**B**)

Figure 8. *Cont.*

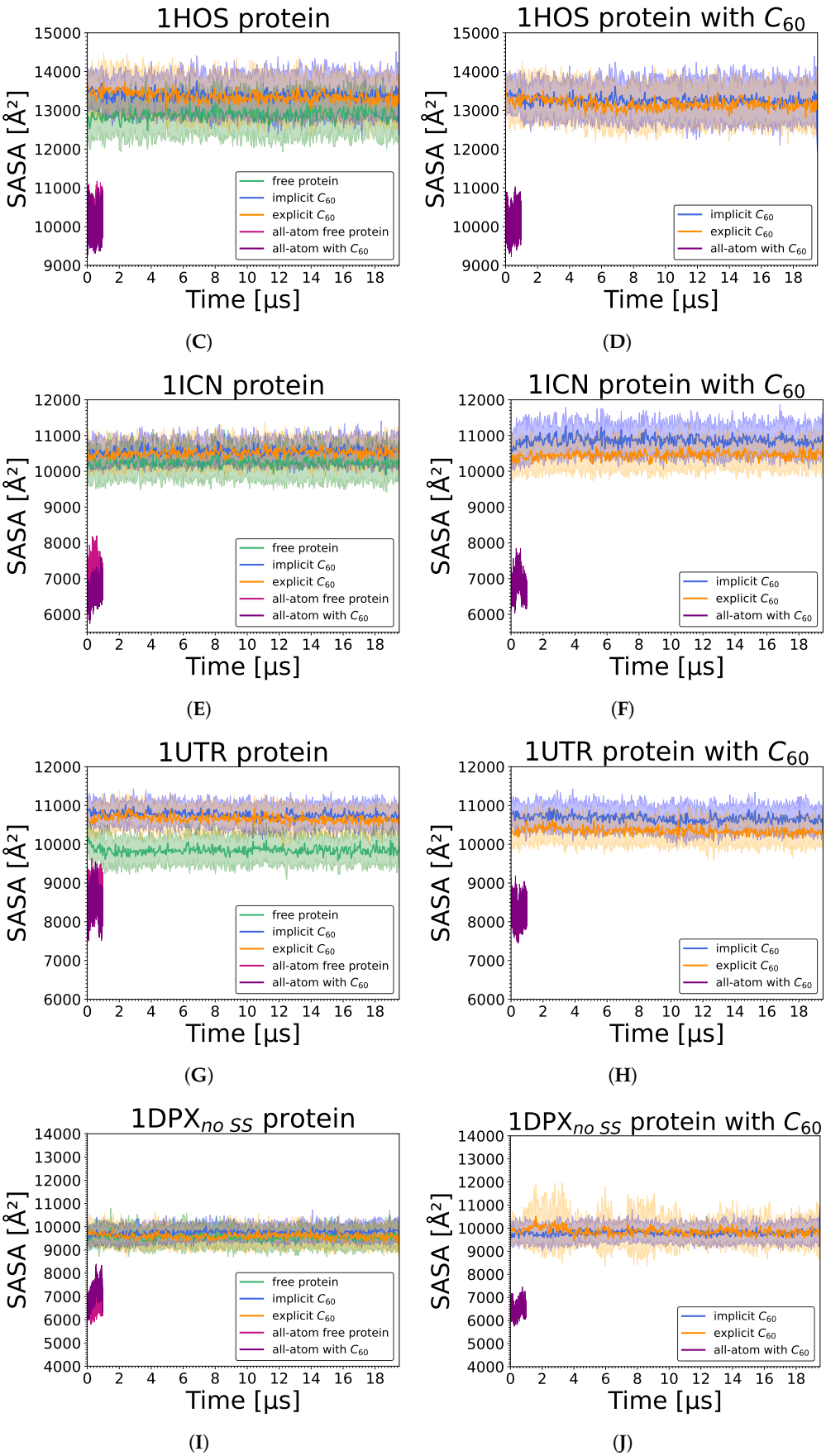

Figure 8. *Cont.*

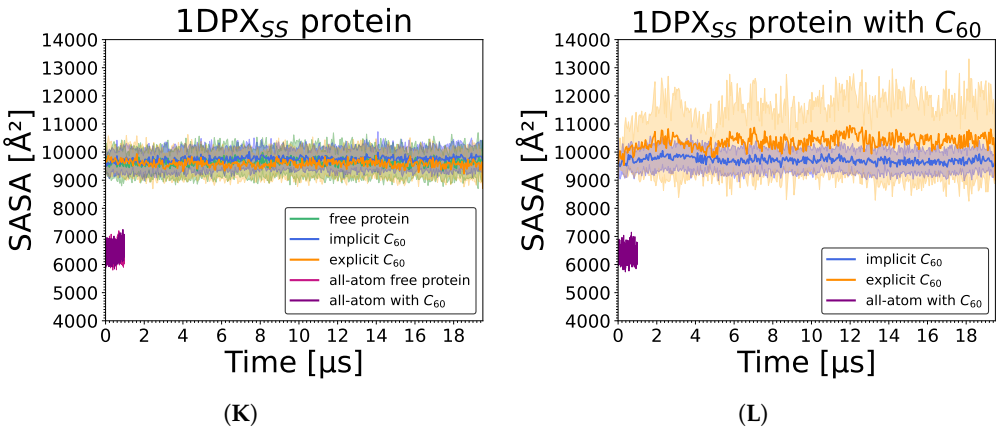

(**K**) (**L**)

Figure 8. SASA values for protein structures (**A**,**C**,**E**,**G**,**I**,**K**) in protein-only, implicit, explicit simulations (averaged over 20 trajectories), and during single all-atom simulations in Amber (without and with C_{60}) and for proteins with C_{60} (**B**,**D**,**F**,**H**,**J**,**L**) in implicit and explicit simulations (averaged over 20 trajectories), and single all-atom simulation in Amber. For protein-only, implicit, and explicit simulations, the straight line represents the average value, while the shaded area along the line corresponds to its standard deviation.

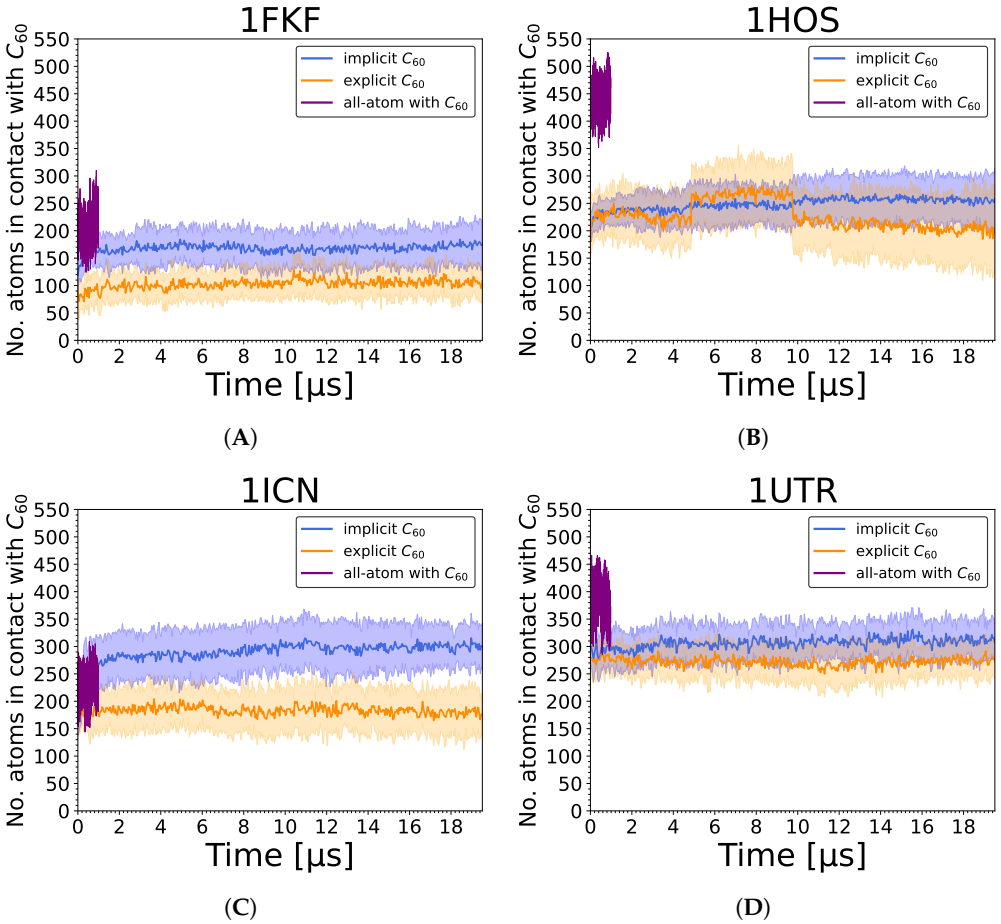

(**A**) (**B**)

(**C**) (**D**)

Figure 9. *Cont.*

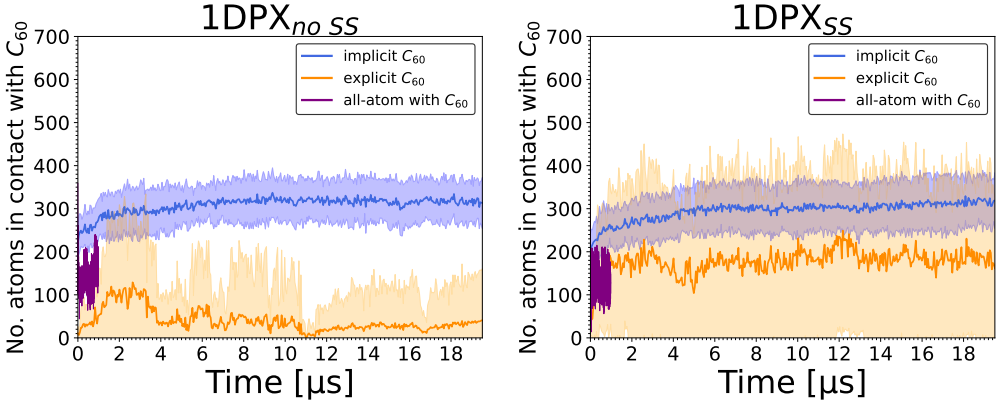

(**E**) (**F**)

Figure 9. Number of atoms in contact with C_{60} during implicit and explicit simulations (averaged over 20 trajectories), and during single all-atom simulation in Amber for (**A**) 1FKF, (**B**) 1HOS, (**C**) 1ICN, (**D**) 1UTR, (**E**) 1DPX$_{no\ SS}$, and (**F**) 1DPX$_{SS}$. For implicit and explicit simulations, the straight line represents the average value, while the shaded area along the line corresponds to its standard deviation.

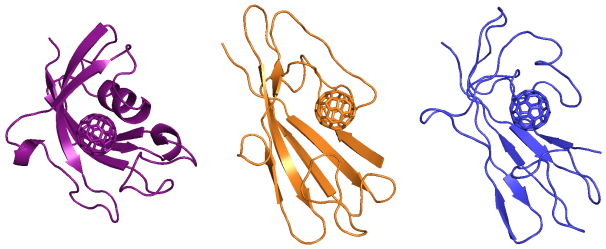

(**A**)

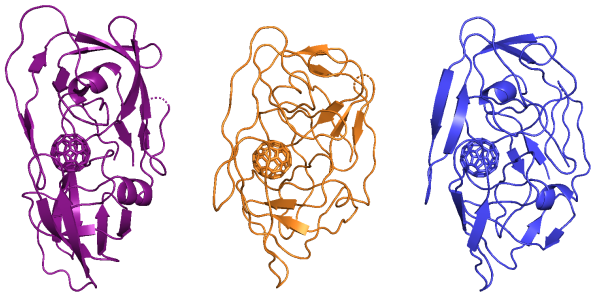

(**B**)

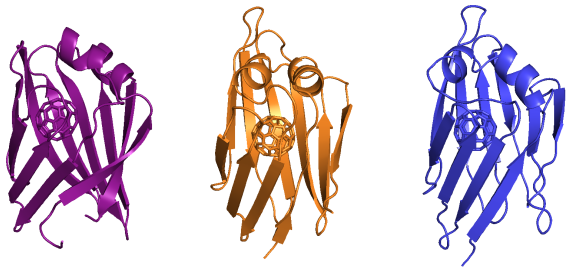

(**C**)

Figure 10. *Cont.*

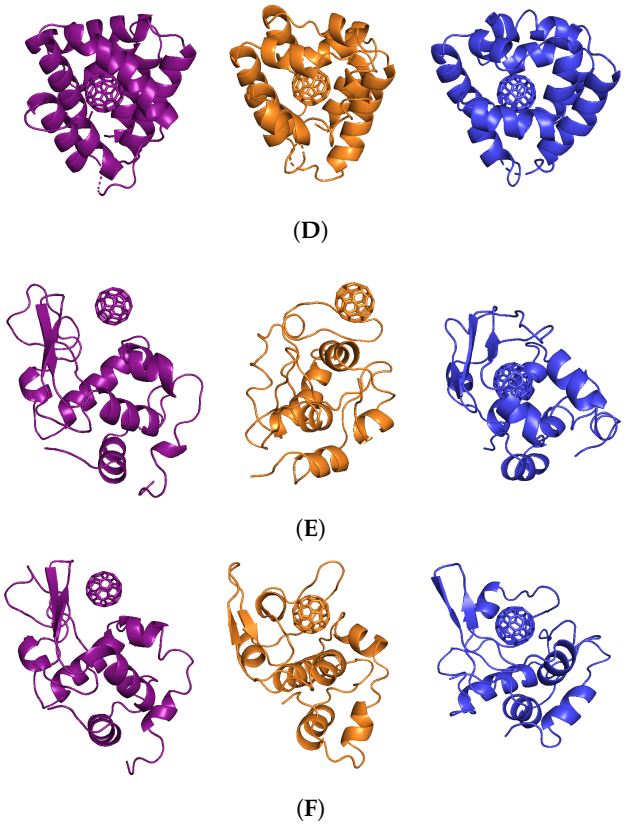

Figure 10. Representative structures of protein with C_{60} from the cluster analysis, where the chosen structure corresponds to the most populated cluster, for (**A**) 1FKF, (**B**) 1HOS, (**C**) 1ICN, (**D**) 1UTR, (**E**) $1DPX_{no\ SS}$, and (**F**) $1DPX_{SS}$. The representatives are shown for all-atom, explicit, and implicit simulations in purple, orange, and blue, respectively.

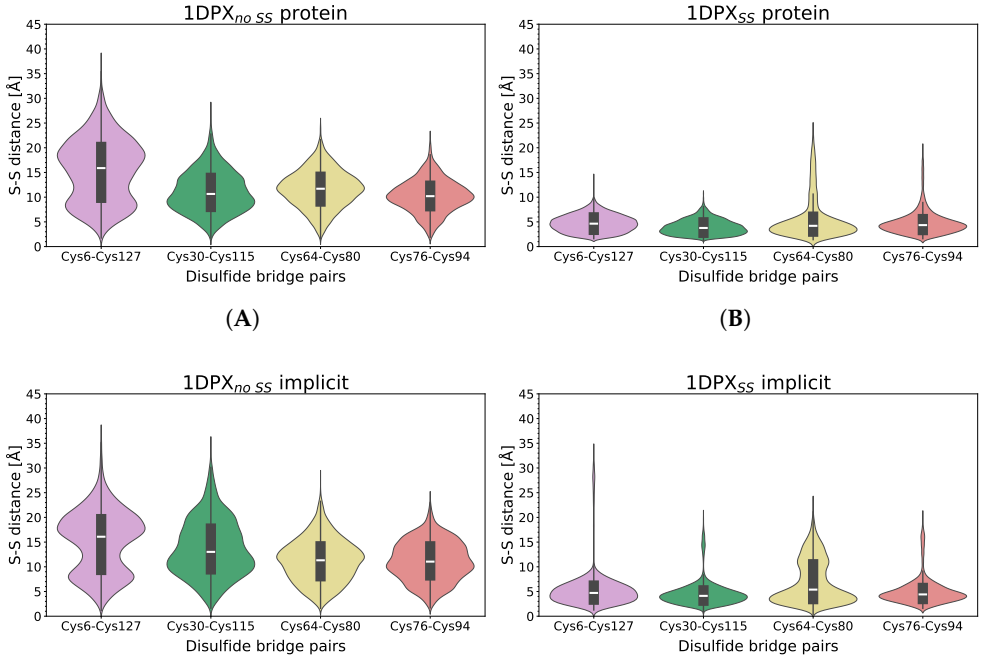

Figure 11. *Cont.*

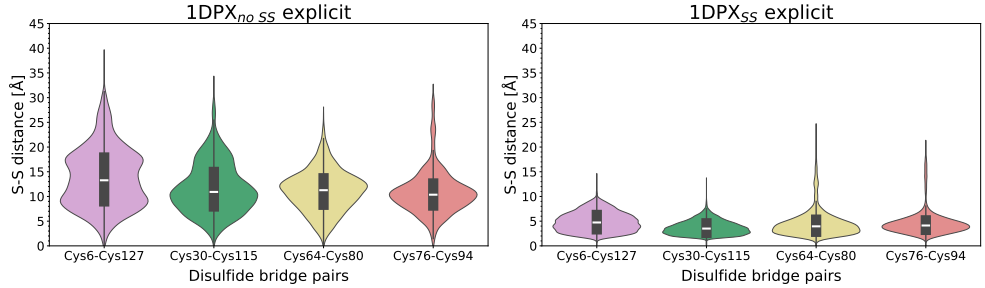

Figure 11. Violin plot of distances between sulfur atoms in UNRES MD simulations of the 1DPX (top row, panels **A**,**B**), with the implicit C_{60} model (middle row, panels **C**,**D**) and with the explicit C_{60} model (bottom row, panels **E**,**F**), with no disulfide bonds (left column, panels **A**,**C**,**E**) and with dynamic treatment of the disulfide bonds (right column, panels **B**,**D**,**F**).

4. Discussion

The results presented in this study demonstrate the successful implementation of both explicit and implicit C_{60} fullerene models into the UNRES coarse-grained force field for molecular dynamics simulations of protein–nanoparticle interactions. The explicit model, representing C_{60} as 20 alanine side chains in a dodecahedral arrangement, showed good agreement with all-atom simulations in terms of predicting protein flexibility, the position of the fullerene in protein binding pockets, and estimated binding energies [36,37,74]. The implicit model, treating C_{60} as an immobile sphere interacting with the protein via a Kihara potential, provided a computationally efficient alternative, although it tended to overestimate binding strength in some cases compared to the explicit model and all-atom simulations [36]. This overestimation of binding strength by the implicit C_{60} model may be attributed to its inherent limitations and simplifications. The lack of flexibility may prevent the nanoparticle from adapting to the protein surface and forming more realistic interactions, potentially leading to an overestimation of binding strength. Furthermore, the implicit model relies on predetermined parameters, such as the interaction potential well depth (ϵ) and distance (σ), which were taken from the phenylalanine side-chain model to approximate C_{60}. These fixed parameters may not be optimal for all protein systems, resulting in inaccuracies in binding energy calculations. To address these limitations, future work will focus on optimizing these parameters to better fit the binding affinities predicted by all-atom methods. This optimization is expected to improve the accuracy of the implicit C_{60} model across a wider range of protein–nanoparticle systems. Additionally, there are ongoing improvements to the UNRES potentials, parameters, and method for reconstructing all-atom models from coarse-grained representations optimized on UNRES models rather than experimental conformations. These advancements are expected to enhance the accuracy of local protein structure predictions.

In this study, all analyses are based on unrestrained UNRES simulations, in which the investigated systems are free to change conformations during trajectories, which allows for a more extensive exploration of the protein conformational space compared to models that rely on restraints or structure-based potentials. By allowing the system to evolve freely during simulations, UNRES can capture a wider range of conformational states and transitions that may be relevant to protein function and dynamics. This approach differs significantly from other popular coarse-grained models, such as MARTINI, which not only applies restraints (elastic network or Go-like potentials) to maintain protein structural stability but also utilizes potentials based on the reference (initial) structure, further biasing possible protein conformational changes and structural stability [51,53]. However, it should be noted that the use of a coarse-grained representation and unbiased, unrestrained trajectories may, in rare cases, lead to an overdestabilization of proteins in some trajectories. Therefore, average properties, rather than single outlying events, should be analyzed to obtain a more accurate understanding of the system's behavior.

Analysis of contact probabilities between C_{60} and protein residues revealed distinct interaction patterns for the different proteins studied. For example, specific binding sites were observed for FK506 binding protein (1FKF), while more generalized interactions were seen for intestinal fatty acid binding protein (1ICN) and uteroglobin (1UTR) [36]. These findings are consistent with previous experimental and computational studies identifying potential C_{60} binding sites on these proteins [23,24,89].

Importantly, the presence of C_{60} did not significantly destabilize any of the proteins in either the explicit or implicit simulations, as evidenced by analysis of RMSD, radius of gyration, and secondary structure [36]. This suggests that C_{60} binding does not induce major conformational changes or denaturation, in agreement with experimental observations [21,38]. However, subtle changes were noted in some cases, such as the slight destabilization of 1FKF and 1ICN in all-atom simulations upon C_{60} binding [36].

The coarse-grained UNRES simulations enabled access to much longer timescales (up to 10 μs) compared to all-atom MD (1 μs), while still capturing key aspects of protein–C_{60} interactions [36]. More importantly, the real-time calculation of 1 μs takes less than an hour on a single CPU core of a standard PC with the UNRES model, while all-atom MD simulations for the investigated systems required 3–5 days on a modern GPU. This time would increase by more than tenfold if a state-of-the-art CPU node with 128 cores were used. This means that with the same computational resources, not only are UNRES coarse-grained simulations about three orders of magnitude longer, but also, two orders of magnitude more trajectories can be run. It should be noted that due to the recent implementation of GPU support in the UNRES package [93], it can now be utilized for simulations. However, owing to its simplified coarse-grained representation, it would primarily offer a significant speed-up for very large systems. This highlights the utility of multiscale approaches leveraging coarse-graining to investigate nanoparticle–biomolecule interactions at experimentally relevant scales that are challenging for conventional all-atom MD [41,44].

The development of accurate coarse-grained force fields is crucial for reliable simulations of protein–nanoparticle interactions. Improvements in parameterization methods, such as maximum likelihood optimization [60], have led to more transferable and robust coarse-grained models. Furthermore, the integration of machine learning techniques, such as graph convolutional networks [94] and diffusion models [95], with coarse-grained simulations has the potential to further enhance the accuracy and efficiency of these methods. Other coarse-grained models have also been successfully applied to study the interactions of fullerenes and their derivatives with lipid membranes [45]. For example, Nisoh et al. used the MARTINI force field to investigate the effects of fullerenes on plasma membrane properties, revealing distinct interaction patterns and potential mechanisms of cellular uptake [45]. It should be noted that our C_{60} model can also be extended through minor modifications, such as altering single or multiple alanine side chains to represent other amino acid residues, like serine in an explicit model or through modifications of σ and ϵ parameters in an implicit model. This adaptation enables the C_{60} model to encompass various fullerene derivatives (FDs), such as fullerenols, thereby greatly expanding the range of simulated systems.

In conclusion, the integration of explicit and implicit C_{60} models into the UNRES force field, coupled with recent advances in coarse-grained modeling and multiscale approaches, provides a powerful framework for investigating protein–nanoparticle interactions at biologically relevant scales. These computational tools, in synergy with experimental techniques, can aid in understanding the mechanisms and consequences of nanoparticle–biomolecule interactions, guiding the design of nanomaterials for biomedical applications. Future work should focus on extending these models to other fullerene derivatives and biomolecular systems, as well as incorporating advanced sampling techniques and machine learning methods to further enhance the accuracy and efficiency of coarse-grained simulations.

5. Conclusions

In this work, explicit and implicit C_{60} fullerene models were successfully integrated into the UNRES coarse-grained force field and applied to study interactions with several proteins without using any restraints, thus allowing for large conformational changes. The explicit model, parameterized based on all-atom simulations, yielded results consistent with all-atom MD in terms of protein flexibility, C_{60} binding poses, and interaction energies. The implicit model provided a more computationally efficient alternative, although it sometimes overestimated binding strength.

Analysis of the simulations revealed protein-specific interaction patterns, with some exhibiting localized C_{60} binding sites and others more generalized interactions. Importantly, C_{60} did not significantly disrupt protein stability in most cases, and even led to an increase in the stability of lysozyme when no disulfide bonds were present. The coarse-grained simulations accessed submillisecond timescales, enabling observation of events beyond the reach of conventional all-atom MD.

Overall, this study demonstrates the utility of coarse-grained MD, specifically the UNRES force field, for investigating protein–nanoparticle interactions. The multiscale approach of integrating insights from all-atom simulations into coarse-grained models can provide a powerful framework for probing these systems at experimentally and physiologically relevant scales. The developed C_{60} models can be readily extended to other carbon nanoparticles, such as fullerene derivatives, and combined with advanced sampling techniques to further explore the mechanisms and consequences of nanoparticle–protein interactions. These computational tools, in synergy with experiments, can aid in understanding the biological effects of nanomaterials and guide the design of nanoparticles for biomedical applications.

Supplementary Materials: The following supporting information can be downloaded at: https://www.mdpi.com/article/10.3390/molecules29091919/s1, Figure S1: Contact probability of nanoparticle interaction centers as a function of time averaged over 20 trajectories for (A) 1FKF, (B) 1HOS, (C) 1ICN, (D) 1UTR, (E) $1DPX_{no\ SS}$, and (F) $1DPX_{SS}$ proteins performed with UNRES force field in simulations with explicitly defined fullerene nanoparticle; Figure S2: Contact probability of protein residues as a function of time averaged over 20 trajectories for (A) 1FKF, (B) 1HOS, (C) 1ICN, (D) 1UTR, (E) $1DPX_{no\ SS}$, and (F) $1DPX_{SS}$ proteins performed with UNRES force field in simulations with explicitly defined fullerene nanoparticle; Figure S3: RMSD values over time for each of 20 trajectory in explicit simulations for (A) $1DPX_{no\ SS}$ and (B) $1DPX_{SS}$ proteins performed with UNRES force field; Table S1: ϵ and σ parameters used for Kihara potential for nanoparticle in implicit form and the Gay–Berne potential parameters ϵ and $\sigma 0_i$ (σ_i) of individual residue i and χ', where $\sigma 0$, (σ) is distance corresponding to the 0 value of $E_{Gay--Berne}$ at side-to-side (head-to-head) orientation from which χ is computed. * Peptide group interacts through LJ potential; a negative ϵ_0 value indicates that both 6 and 12 terms are repulsive.

Author Contributions: Conceptualization, M.A.K. and P.K.; methodology, P.K. and A.K.S.; software, A.K.S.; validation, P.K. and A.K.S.; formal analysis, N.H.R.; investigation, N.H.R.; resources, A.K.S. and P.K.; data curation, N.H.R.; writing—original draft preparation, N.H.R., A.K.S. and P.K.; writing—review and editing, N.H.R., A.K.S. and P.K.; visualization, N.H.R.; supervision, A.K.S. and P.K.; project administration, A.K.S. and P.K.; funding acquisition, P.K. All authors have read and agreed to the published version of the manuscript.

Funding: This research was funded by the National Science Centre, Poland, under SONATA No 2019/35/D/ST4/03156.

Data Availability Statement: Data are contained within the article and Supplementary Materials.

Acknowledgments: We thank Cezary Czaplewski from the University of Gdańsk for his helpful consultation on the calculation of binding energy. Grammarly, GPT-3.5, and the Claude 3 OPUS models were used solely to ensure a high level of grammatical correctness.

Conflicts of Interest: The authors declare no conflicts of interest.

References

1. Baig, N.; Kammakakam, I.; Falath, W. Nanomaterials: A review of synthesis methods, properties, recent progress, and challenges. *Mater. Adv.* **2021**, *2*, 1821–1871. [CrossRef]
2. Bayda, S.; Adeel, M.; Tuccinardi, T.; Cordani, M.; Rizzolio, F. The History of Nanoscience and Nanotechnology: From Chemical–Physical Applications to Nanomedicine. *Molecules* **2020**, *25*, 112. [CrossRef] [PubMed]
3. Mauter, M.S.; Elimelech, M. Environmental Applications of Carbon-Based Nanomaterials. *Environ. Sci. Technol.* **2008**, *42*, 5843–5859. [CrossRef] [PubMed]
4. Hirsch, A. The Chemistry of the Fullerenes: An Overview. *Angew. Chem.* **1993**, *32*, 1138–1141. [CrossRef]
5. Prato, M. [60]Fullerene chemistry for materials science applications. *J. Mater. Chem.* **1997**, *7*, 1097–1109. [CrossRef]
6. Kroto, H.; Heath, J.; O'Brien, S. C60: Buckminsterfullerene. *Nature* **1985**, *318*, 162–163. [CrossRef]
7. Cui, F.; Luo, C.; Dong, J. Dimerization of C60 molecules within the single-walled carbon nanotube. *Phys. Lett. A* **2004**, *327*, 55–60. [CrossRef]
8. Baker, G.; Gupta, A.; Clark, M.; Valenzuela, B.; Staska, L.; Harbo, S.; Pierce, J.; Dill, J. Inhalation toxicity and lung toxicokinetics of C60 fullerene nanoparticles and microparticles. *Toxicol. Sci.* **2008**, *101*, 122–131. [CrossRef] [PubMed]
9. Buseck, P.R. Geological fullerenes: Review and analysis. *Earth Planet. Sci. Lett.* **2002**, *203*, 781–792. [CrossRef]
10. Sayers, B.C.; Walker, N.J.; Roycroft, J.H.; Germolec, D.R.; Baker, G.L.; Clark, M.L.; Hayden, B.K.; DeFord, H.; Dill, J.A.; Gupta, A.; et al. Lung deposition and clearance of microparticle and nanoparticle C60 fullerene aggregates in B6C3F1 mice and Wistar Han rats following nose-only inhalation for 13 weeks. *Toxicology* **2016**, *339*, 87–96. [CrossRef]
11. Hendren, C.O.; Mesnard, X.; Dröge, J.; Wiesner, M.R. Estimating Production Data for Five Engineered Nanomaterials As a Basis for Exposure Assessment. *Environ. Sci. Technol.* **2011**, *45*, 2562–2569. [CrossRef] [PubMed]
12. Junaid, M.; Almuqri, E.; Liu, J.; Zhang, H. Analyses of the Binding between Water Soluble C60 Derivatives and Potential Drug Targets through a Molecular Docking Approach. *PLoS ONE* **2016**, *11*, e0147761. [CrossRef] [PubMed]
13. Thompson, B.C.; Fréchet, J.M.J. Polymer-fullerene composite solar cells. *Angew. Chem.* **2008**, *47*, 58–77. [CrossRef] [PubMed]
14. Shetti, N.P.; Mishra, A.; Basu, S.; Aminabhavi, T.M. Versatile fullerenes as sensor materials. *Mater. Today Chem.* **2021**, *20*, 100454. [CrossRef]
15. Panwar, N.; Soehartono, A.M.; Chan, K.K.; Zeng, S.; Xu, G.; Qu, J.; Coquet, P.; Yong, K.T.; Chen, X. Nanocarbons for Biology and Medicine: Sensing, Imaging, and Drug Delivery. *Chem. Rev.* **2019**, *119*, 9559–9656. [CrossRef] [PubMed]
16. Mousavi, S.Z.; Nafisi, S.; Maibach, H.I. Fullerene nanoparticle in dermatological and cosmetic applications. *Nanomed. Nanotechnol. Biol. Med.* **2017**, *13*, 1071–1087. [CrossRef] [PubMed]
17. Kazemzadeh, H.; Mozafari, M. Fullerene-based delivery systems. *Drug Discov. Today* **2019**, *24*, 898–905. [CrossRef]
18. Dellinger, A.; Zhou, Z.; Connor, J.; Madhankumar, A.; Pamujula, S.; Sayes, C.M.; Kepley, C.L. Application of fullerenes in nanomedicine: An update. *Nanomed.* **2013**, *8*, 1191–1208. [CrossRef] [PubMed]
19. Utsunomiya, S.; Jensen, K.A.; Keeler, G.J.; Ewing, R.C. Uraninite and Fullerene in Atmospheric Particulates. *Environ. Sci. Technol.* **2002**, *36*, 4943–4947. [CrossRef]
20. Aschberger, K.; Johnston, H.J.; Stone, V.; Aitken, R.J.; Tran, C.L.; Hankin, S.M.; Peters, S.A.; Christensen, F.M. Review of fullerene toxicity and exposure—Appraisal of a human health risk assessment, based on open literature. *Regul. Toxicol. Pharmacol.* **2010**, *58*, 455–473. [CrossRef]
21. Johnston, H.J.; Hutchison, G.R.; Christensen, F.M.; Aschberger, K.; Stone, V. The biological mechanisms and physicochemical characteristics responsible for driving fullerene toxicity. *Toxicol. Sci.* **2010**, *114*, 162–182. [CrossRef] [PubMed]
22. Ha, Y.; Wang, X.; Liljestr, H.M.; Maynard, J.A.; Katz, L.E. Elucidating the mechanism of cellular uptake of fullerene nanoparticles. *Environ. Eng. Res.* **2022**, *27*, 200658. [CrossRef]
23. Friedman, S.H.; DeCamp, D.L.; Sijbesma, R.P.; Srdanov, G.; Wudl, F.; Kenyon, G.L. Inhibition of the HIV-1 protease by fullerene derivatives: Model building studies and experimental verification. *J. Am. Chem. Soc.* **1993**, *115*, 6506–6509. [CrossRef]
24. Chen, B.; Wilson, S.; Das, M.; Coughlin, D.; Erlanger, B. Antigenicity of fullerenes: Antibodies specific for fullerenes and their characteristics. *Proc. Nat. Acad. Sci. USA* **1998**, *95*, 10809–10813. [CrossRef] [PubMed]
25. Ueng, T.H.; Kang, J.J.; Wang, H.W.; Cheng, Y.W.; Chiang, L.Y. Suppression of microsomal cytochrome P450-dependent monooxygenases and mitochondrial oxidative phosphorylation by fullerenol, a polyhydroxylated fullerene C60. *Toxicol. Lett.* **1997**, *93*, 29–37. [CrossRef] [PubMed]
26. Simic-Krstic, J. Effects of C60(OH)24 on Microtubule Assembly. *Arch. Oncol.* **1997**, *5*, 143–147.
27. Jin, H.; Chen, W.; Tang, X.; Chiang, L.; Yang, C.; Schloss, J.; Wu, J. Polyhydroxylated C60, fullerenols, as glutamate receptor antagonists and neuroprotective agents. *J. Neurosci. Res.* **2000**, *62*, 600–607. [CrossRef] [PubMed]
28. Yang, S.T.; Wang, H.; Guo, L.; Gao, Y.; Liu, Y.; Cao, A. Interaction of fullerenol with lysozyme investigated by experimental and computational approaches. *Nanotechnology* **2008**, *19*, 395101. [CrossRef]
29. Tokuyama, H.; Yamago, S.; Nakamura, E.; Shiraki, T.; Sugiura, Y. Photoinduced biochemical activity of fullerene carboxylic acid. *J. Am. Chem. Soc.* **1993**, *115*, 7918–7919. [CrossRef]
30. Nakamura, E.; Tokuyama, H.; Yamago, S.; Shiraki, T.; Sugiura, Y. Biological Activity of Water-Soluble Fullerenes. Structural Dependence of DNA Cleavage, Cytotoxicity, and Enzyme Inhibitory Activities Including HIV-Protease Inhibition. *Bull. Chem. Soc. Jpn.* **1996**, *69*, 2143–2151. [CrossRef]

31. Wolff, D.J.; Mialkowski, K.; Richardson, C.F.; Wilson, S.R. C60-Fullerene monomalonate adducts selectively inactivate neuronal nitric oxide synthase by uncoupling the formation of reactive oxygen intermediates from nitric oxide production. *Biochemistry* **2001**, *40*, 37–45. [CrossRef] [PubMed]
32. Park, K.H.; Chhowalla, M.; Iqbal, Z.; Sesti, F. Single-walled Carbon Nanotubes Are a New Class of Ion Channel Blockers. *J. Biol. Chem.* **2003**, *278*, 50212–50216. [CrossRef]
33. Belgorodsky, B.; Fadeev, L.; Ittah, V.; Benyamini, H.; Zelner, S.; Huppert, D.; Kotlyar, A.B.; Gozin, M. Formation and Characterization of Stable Human Serum Albumin-Tris-malonic Acid [C60]Fullerene Complex. *Bioconj. Chem.* **2005**, *16*, 1058–1062. [CrossRef] [PubMed]
34. Belgorodsky, B.; Fadeev, L.; Kolsenik, J.; Gozin, M. Formation of a Soluble Stable Complex between Pristine C60-Fullerene and a Native Blood Protein. *ChemBioChem* **2006**, *7*, 1783–1789. [CrossRef]
35. Pastorin, G.; Marchesan, S.; Hoebeke, J.; Da Ros, T.; Ehret-Sabatier, L.; Briand, J.P.; Prato, M.; Bianco, A. Design and activity of cationic fullerene derivatives as inhibitors of acetylcholinesterase. *Org. Biomol. Chem.* **2006**, *4*, 2556–2562. [CrossRef] [PubMed]
36. Calvaresi, M.; Zerbetto, F. Baiting Proteins with C60. *ACS Nano* **2010**, *4*, 2283–2299. [CrossRef]
37. Ahmed, L.; Rasulev, B.; Kar, S.; Krupa, P.; Mozolewska, M.A.; Leszczynski, J. Inhibitors or toxins? Large library target-specific screening of fullerene-based nanoparticles for drug design purpose. *Nanoscale* **2017**, *9*, 10263–10276. [CrossRef]
38. Sayes, C.M.; Fortner, J.D.; Guo, W.; Lyon, D.A.; Boyd, A.M.; Ausman, K.D.; Colvin, V.L. The Differential Cytotoxicity of Water-Soluble Fullerenes. *Nano Lett.* **2004**, *4*, 1881–1887. [CrossRef]
39. Sayes, C.M.; Marchione, A.A.; Reed, K.L.; Warheit, D.B. Comparative Pulmonary Toxicity Assessments of C60Water Suspensions in Rats: Few Differences in Fullerene Toxicity in Vivo in Contrast to in Vitro Profiles. *Nano Lett.* **2007**, *7*, 2399–2406. [CrossRef] [PubMed]
40. Caldeira, D.A.; Mesquita, F.M.; Pinheiro, F.G.; Oliveira, D.F.; Oliveira, L.F.; Nascimento, J.H.; Takiya, C.M.; Maciel, L.; Zin, W.A. Acute exposure to C60 fullerene damages pulmonary mitochondrial function and mechanics. *Nanotoxicology* **2021**, *15*, 352–365. [CrossRef] [PubMed]
41. Ghavanloo, E.; Rafii-Tabar, H.; Kausar, A.; Giannopoulos, G.I.; Fazelzadeh, S.A. Experimental and computational physics of fullerenes and their nanocomposites: Synthesis, thermo-mechanical characteristics and nanomedicine applications. *Phys. Rep.* **2023**, *996*, 1–116. [CrossRef]
42. Nasraoui, S.; Ben Brahim, N.; Bel Haj Mohamed, N.; Ben Chaabane, R.; Allouche, A. Theoretical and experimental investigation on ligands-CdS clusters interactions: Influence of solvent. *J. Mol. Struct.* **2018**, *1173*, 894–902. [CrossRef]
43. Lin, P.C.; Lin, S.; Wang, P.C.; Sridhar, R. Techniques for physicochemical characterization of nanomaterials. *Biotech. Adv.* **2014**, *32*, 711–726. [CrossRef] [PubMed]
44. Rodríguez-Castillo, M.; Lugo-Preciado, G.; Laurencin, D.; Tielens, F.; van der Lee, A.; Clément, S.; Guari, Y.; López-de Luzuriaga, J.M.; Monge, M.; Remacle, F.; et al. Experimental and Theoretical Study of the Reactivity of Gold Nanoparticles Towards Benzimidazole-2-ylidene Ligands. *Chem. Eur. J.* **2016**, *22*, 10446–10458. [CrossRef] [PubMed]
45. Nisoh, N.; Jarerattanachat, V.; Karttunen, M.; Wong-ekkabut, J. Fullerenes' Interactions with Plasma Membranes: Insight from the MD Simulations. *Biomolecules* **2022**, *12*, 639. [CrossRef] [PubMed]
46. Tavanti, F.; Pedone, A.; Menziani, M.C. Multiscale Molecular Dynamics Simulation of Multiple Protein Adsorption on Gold Nanoparticles. *Int. J. Mol. Sci.* **2019**, *20*, 3539. [CrossRef] [PubMed]
47. Wallace, E.J.; Sansom, M.S.P. Carbon nanotube self-assembly with lipids and detergent: A molecular dynamics study. *Nanotechnology* **2008**, *20*, 045101. [CrossRef] [PubMed]
48. D'Rozario, R.S.G.; Wee, C.L.; Wallace, E.J.; Sansom, M.S.P. The interaction of C60 and its derivatives with a lipid bilayer via molecular dynamics simulations. *Nanotechnology* **2009**, *20*, 115102. [CrossRef] [PubMed]
49. Lai, K.; Wang, B.; Zhang, Y.; Zheng, Y. Computer simulation study of nanoparticle interaction with a lipid membrane under mechanical stress. *Phys. Chem. Chem. Phys.* **2013**, *15*, 270–278. [CrossRef]
50. Lin, J.Q.; Zheng, Y.G.; Zhang, H.W.; Chen, Z. A Simulation Study on Nanoscale Holes Generated by Gold Nanoparticles on Negative Lipid Bilayers. *Langmuir* **2011**, *27*, 8323–8332. [CrossRef]
51. Alessandri, R.; Thallmair, S.; Herrero, C.G.; Mera-Adasme, R.; Marrink, S.J.; Souza, P.C.T. A Practical Introduction to Martini 3 and its Application to Protein-Ligand Binding Simulations. In *A Practical Guide to Recent Advances in Multiscale Modeling and Simulation of Biomolecules*; AIP Publishing LLC: Melville, NY, USA, 2023. [CrossRef]
52. Borges-Araújo, L.; Patmanidis, I.; Singh, A.P.; Santos, L.H.S.; Sieradzan, A.K.; Vanni, S.; Czaplewski, C.; Pantano, S.; Shinoda, W.; Monticelli, L.; et al. Pragmatic Coarse-Graining of Proteins: Models and Applications. *J. Chem. Theory Comput.* **2023**, *19*, 7112–7135. [CrossRef] [PubMed]
53. Marrink, S.J.; Monticelli, L.; Melo, M.N.; Alessandri, R.; Tieleman, D.P.; Souza, P.C.T. Two decades of Martini: Better beads, broader scope. *WIREs Comput. Mol. Sci.* **2023**, *13*, e1620, [CrossRef]
54. Periole, X.; Cavalli, M.; Marrink, S.J.; Ceruso, M.A. Combining an elastic network with a coarse-grained molecular force field: Structure, dynamics, and intermolecular recognition. *J. Chem. Theory Comput.* **2009**, *5*, 2531–2543. [CrossRef] [PubMed]
55. Poma, A.B.; Cieplak, M.; Theodorakis, P.E. Combining the MARTINI and structure-based coarse-grained approaches for the molecular dynamics studies of conformational transitions in proteins. *J. Chem. Theory Comput.* **2017**, *13*, 1366–1374. [CrossRef] [PubMed]

56. Liwo, A.; Baranowski, M.; Czaplewski, C.; Gołaś, E.; He, Y.; Jagieła, D.; Krupa, P.; Maciejczyk, M.; Makowski, M.; Mozolewska, M.A.; et al. A unified coarse-grained model of biological macromolecules based on mean-field multipole-multipole interactions. *J. Mol. Model.* **2014**, *20*, 2306. [CrossRef]
57. Sieradzan, A.K.; Czaplewski, C.; Krupa, P.; Mozolewska, M.A.; Karczyńska, A.S.; Lipska, A.G.; Lubecka, E.A.; Gołąś, E.; Wirecki, T.; Makowski, M.; et al. Modeling the Structure, Dynamics, and Transformations of Proteins with the UNRES Force Field. In *Protein Folding: Methods and Protocols*; Muñoz, V., Ed.; Springer: New York, NY, USA, 2022; pp. 399–416. [CrossRef]
58. Chinchio, M.; Czaplewski, C.; Liwo, A.; Ołdziej, S.; Scheraga, H.A. Dynamic Formation and Breaking of Disulfide Bonds in Molecular Dynamics Simulations with the UNRES Force Field. *J. Chem. Theory Comput.* **2007**, *3*, 1236–1248. [CrossRef] [PubMed]
59. Liwo, A.; Czaplewski, C.; Pillardy, J.; Scheraga, H.A. Cumulant-based expressions for the multibody terms for the correlation between local and electrostatic interactions in the united-residue force field. *J. Chem. Phys.* **2001**, *115*, 2323–2347. [CrossRef]
60. Krupa, P.; Hałabis, A.; Żmudzińska, W.; Ołdziej, S.; Scheraga, H.A.; Liwo, A. Maximum Likelihood Calibration of the UNRES Force Field for Simulation of Protein Structure and Dynamics. *J. Chem. Inf. Model.* **2017**, *57*, 2364–2377. [CrossRef] [PubMed]
61. Liwo, A.; Khalili, M.; Czaplewski, C.; Kalinowski, S.; Ołdziej, S.; Wachucik, K.; Scheraga, H.A. Modification and Optimization of the United-Residue (UNRES) Potential Energy Function for Canonical Simulations. I. Temperature Dependence of the Effective Energy Function and Tests of the Optimization Method with Single Training Proteins. *J. Phys. Chem. B* **2007**, *111*, 260–285. [CrossRef]
62. He, Y.; Mozolewska, M.A.; Krupa, P.; Sieradzan, A.K.; Wirecki, T.K.; Liwo, A.; Kachlishvili, K.; Rackovsky, S.; Jagieła, D.; Scheraga, H.A.; et al. Lessons from application of the UNRES force field to predictions of structures of CASP10 targets. *Proc. Nat. Acad. Sci. USA* **2013**, *110*, 14936–14941. [CrossRef]
63. Krupa, P.; Mozolewska, M.A.; Wiśniewska, M.; Yin, Y.; He, Y.; Sieradzan, A.K.; Ganzynkowicz, R.; Lipska, A.G.; Karczyńska, A.; Ślusarz, M.; et al. Performance of protein-structure predictions with the physics-based UNRES force field in CASP11. *Bioinformatics* **2016**, *32*, 3270–3278. [CrossRef]
64. Lubecka, E.A.; Karczyńska, A.S.; Lipska, A.G.; Sieradzan, A.K.; Zieba, K.; Sikorska, C.; Uciechowska, U.; Samsonov, S.A.; Krupa, P.; Mozolewska, M.A.; et al. Evaluation of the scale-consistent UNRES force field in template-free prediction of protein structures in the CASP13 experiment. *J. Mol. Graph. Modell.* **2019**, *92*, 154–166. [CrossRef]
65. Karczyńska, A.S.; Zieba, K.; Uciechowska, U.; Mozolewska, M.A.; Krupa, P.; Lubecka, E.A.; Lipska, A.G.; Sikorska, C.; Samsonov, S.A.; Sieradzan, A.K.; et al. Improved Consensus-Fragment Selection in Template-Assisted Prediction of Protein Structures with the UNRES Force Field in CASP13. *J. Chem. Inf. Model.* **2020**, *60*, 1844–1864. [CrossRef] [PubMed]
66. Zhou, R.; Maisuradze, G.G.; Suñol, D.; Liwo, A.; Scheraga, H.A. Folding kinetics of WW domains with the united residue force field for bridging microscopic motions and experimental measurements. *Proc. Nat. Acad. Sci. USA* **2014**, *111*, 18243–18248. [CrossRef] [PubMed]
67. Maisuradze, G.G.; Senet, P.; Czaplewski, C.; Liwo, A.; Scheraga, H.A. Investigation of Protein Folding by Coarse-Grained Molecular Dynamics with the UNRES Force Field. *J. Phys. Chem. A* **2010**, *114*, 4471–4485. [CrossRef] [PubMed]
68. Nguyen, H.L.; Krupa, P.; Hai, N.M.; Linh, H.Q.; Li, M.S. Structure and Physicochemical Properties of the Aβ42 Tetramer: Multiscale Molecular Dynamics Simulations. *J. Phys. Chem. B* **2019**, *123*, 7253–7269. [CrossRef] [PubMed]
69. Lipska, A.G.; Sieradzan, A.K.; Czaplewski, C.; Lipińska, A.D.; Ocetkiewicz, K.M.; Proficz, J.; Czarnul, P.; Krawczyk, H.; Liwo, A. Long-time scale simulations of virus-like particles from three human-norovirus strains. *J. Comput. Chem.* **2023**, 44, 1470–1483. [CrossRef] [PubMed]
70. Sieradzan, A.K.; Mozolewska, M.A. Extension of coarse-grained UNRES force field to treat carbon nanotubes. *J. Mol. Model.* **2018**, *24*, 121. [CrossRef] [PubMed]
71. Zaborowski, B.; Jagieła, D.; Czaplewski, C.; Hałabis, A.; Lewandowska, A.; Żmudzińska, W.; Liwo, A. A Maximum-Likelihood Approach to Force-Field Calibration. *J. Chem. Inf. Model.* **2015**, *55*, 2050–2070. [CrossRef]
72. Makowski, M.; Liwo, A.; Scheraga, H.A. Simple physics-based analytical formulas for the potentials of mean force of the interaction of amino acid side chains in water. VII. Charged–hydrophobic/polar and polar–hydrophobic/polar side chains. *J. Phys. Chem. B* **2017**, *121*, 379–390. [CrossRef]
73. Kihara, T. The second virial coefficient of non-spherical molecules. *J. Phys. Soc. Jpn.* **1951**, *6*, 289–296. [CrossRef]
74. Giełdoń, A.; Witt, M.M.; Gajewicz, A.; Puzyn, T. Rapid insight into C60 influence on biological functions of proteins. *Struct. Chem.* **2017**, *28*, 1775–1788. [CrossRef]
75. Krupa, P.; Sieradzan, A.K.; Mozolewska, M.A.; Li, H.; Liwo, A.; Scheraga, H.A. Dynamics of Disulfide-Bond Disruption and Formation in the Thermal Unfolding of Ribonuclease A. *J. Chem. Theory Comput.* **2017**, *13*, 5721–5730. [CrossRef] [PubMed]
76. Gay, D.M. Algorithm 611: Subroutines for Unconstrained Minimization Using a Model/Trust-Region Approach. *ACM Trans. Math. Softw.* **1983**, *9*, 503–524. [CrossRef]
77. Antoniak, A.; Biskupek, I.; Bojarski, K.K.; Czaplewski, C.; Giełdoń, A.; Kogut, M.; Kogut, M.M.; Krupa, P.; Lipska, A.G.; Liwo, A.; et al. Modeling protein structures with the coarse-grained UNRES force field in the CASP14 experiment. *J. Mol. Graph. Modell.* **2021**, *108*, 108008. [CrossRef]
78. Case, D.; Aktulga, H.; Belfon, K.; Ben-Shalom, I.; Berryman, J.; Brozell, S.; Cerutti, D.; Cheatham, T.I.; Cisneros, G.; Cruzeiro, V.; et al. *Amber 2023*; University of California, San Francisco: San Francisco, CA, USA, 2023.

79. Tian, C.; Kasavajhala, K.; Belfon, K.A.A.; Raguette, L.; Huang, H.; Migues, A.N.; Bickel, J.; Wang, Y.; Pincay, J.; Wu, Q.; et al. ff19SB: Amino-Acid-Specific Protein Backbone Parameters Trained against Quantum Mechanics Energy Surfaces in Solution. *J. Chem. Theory Comput.* **2020**, *16*, 528–552. [CrossRef] [PubMed]
80. Wang, J.; Wolf, R.M.; Caldwell, J.W.; Kollman, P.A.; Case, D.A. Development and testing of a general amber force field. *J. Comput. Chem.* **2004**, *25*, 1157–1174. [CrossRef]
81. Izadi, S.; Anandakrishnan, R.; Onufriev, A.V. Building Water Models: A Different Approach. *J. Phys. Chem. Lett.* **2014**, *5*, 3863–3871. [CrossRef] [PubMed]
82. Case, D.A.; Aktulga, H.M.; Belfon, K.; Cerutti, D.S.; Cisneros, G.A.; Cruzeiro, V.W.D.; Forouzesh, N.; Giese, T.J.; Götz, A.W.; Gohlke, H.; et al. AmberTools. *J. Chem. Inf. Model.* **2023**, *63*, 6183–6191. [CrossRef]
83. Nguyen, H.; Roe, D.R.; Simmerling, C. Improved Generalized Born Solvent Model Parameters for Protein Simulations. *J. Chem. Theory Comput.* **2013**, *9*, 2020–2034. [CrossRef]
84. Rotkiewicz, P.; Skolnick, J. Fast procedure for reconstruction of full-atom protein models from reduced representations. *J. Comput. Chem.* **2008**, *29*, 1460–1465. [CrossRef] [PubMed]
85. Roe, D.R.; Cheatham, T.E.I. PTRAJ and CPPTRAJ: Software for Processing and Analysis of Molecular Dynamics Trajectory Data. *J. Chem. Theory Comput.* **2013**, *9*, 3084–3095. [CrossRef]
86. Duyne, G.D.V.; Standaert, R.F.; Karplus, P.A.; Schreiber, S.L.; Clardy, J. Atomic Structure of FKBP-FK506, an Immunophilin-Immunosuppressant Complex. *Science* **1991**, *252*, 839–842. [CrossRef]
87. Badaya, A.; Sasidhar, Y.U. Inhibition of the activity of HIV-1 protease through antibody binding and mutations probed by molecular dynamics simulations. *Sci. Rep.* **2020**, *10*, 5501. [CrossRef]
88. Miller, M.; Schneider, J.; Sathyanarayana, B.K.; Toth, M.V.; Marshall, G.R.; Clawson, L.; Selk, L.; Kent, S.B.; Wlodawer, A. Structure of complex of synthetic HIV-1 protease with a substrate-based inhibitor at 2.3 A resolution. *Science* **1989**, *246*, 1149–1152. [CrossRef]
89. Likić, V.A.; Prendergast, F.G. Structure and dynamics of the fatty acid binding cavity in apo rat intestinal fatty acid binding protein. *Protein Sci.* **1999**, *8*, 1649–1657. [CrossRef]
90. Härd, T.; Barnes, H.J.; Larsson, C.; Gustafsson, J.Å.; Lund, J. Solution structure of a mammalian PCB-binding protein in complex with a PCB. *Nat. Struct. Mol. Biol.* **1995**, *2*, 983–989. [CrossRef]
91. Lipska, A.G.; Sieradzan, A.K.; Krupa, P.; Mozolewska, M.A.; D'Auria, S.; Liwo, A. Studies of conformational changes of an arginine-binding protein from Thermotoga maritima in the presence and absence of ligand via molecular dynamics simulations with the coarse-grained UNRES force field. *J. Mol. Model.* **2015**, *21*, 64. [CrossRef]
92. Krupa, P.; Karczyńska, A.S.; Mozolewska, M.A.; Liwo, A.; Czaplewski, C. UNRES-Dock—Protein–protein and peptide–protein docking by coarse-grained replica-exchange MD simulations. *Bioinformatics* **2020**, *37*, 1613–1615. [CrossRef] [PubMed]
93. Ocetkiewicz, K.M.; Czaplewski, C.; Krawczyk, H.; Lipska, A.G.; Liwo, A.; Proficz, J.; Sieradzan, A.K.; Czarnul, P. UNRES-GPU for physics-based coarse-grained simulations of protein systems at biological time- and size-scales. *Bioinformatics* **2023**, *39*, btad391. [CrossRef] [PubMed]
94. Wang, Y.; Jiao, Q.; Wang, J.; Cai, X.; Zhao, W.; Cui, X. Prediction of protein-ligand binding affinity with deep learning. *Comput. Struct. Biotechnol. J.* **2023**, *21*, 5796–5806. [CrossRef]
95. Hoogeboom, E.; Satorras, V.G.; Vignac, C.; Welling, M. Equivariant Diffusion for Molecule Generation in 3D. *arXiv* **2022**, arXiv:2203.17003.